

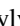









## Numerical simulations of granular dam break: Comparison between discrete element, Navier-Stokes, and thin-layer models

Hugo A. Martin <sup>1,2,\*</sup>, Marc Peruzzetto <sup>3,1</sup>, Sylvain Viroulet <sup>4,1</sup>, Anne Mangeney <sup>1,5</sup>, Pierre-Yves Lagrée <sup>6</sup>, Stéphane Popinet <sup>6</sup>, Bertrand Maury <sup>7,8</sup>, Aline Lefebvre-Lepot <sup>9</sup>, Yvon Maday <sup>2,5</sup> and François Bouchut <sup>10</sup>

<sup>1</sup>Université Paris Cité, Institut de physique du globe de Paris, CNRS, F-75005 Paris, France

<sup>2</sup>Sorbonne Université, CNRS, Université Paris Cité, Laboratoire Jacques-Louis Lions (LJLL), F-75005 Paris, France

<sup>3</sup>BRGM, F-45060 Orléans, France

<sup>4</sup>Institut de Mécanique des Fluides de Toulouse (IMFT), Université de Toulouse, CNRS-INPT-UPS, Toulouse, France

<sup>5</sup>Institut Universitaire de France (IUF), 75231 Paris Cedex 05, France

<sup>6</sup>Institut Jean le Rond d'Alembert, Sorbonne Université, CNRS UMR 7190, F-75005 Paris, France

<sup>7</sup>Département de Mathématiques Appliquées, École Normale Supérieure, Université PSL, 75005 Paris, France

<sup>8</sup>Laboratoire de Mathématiques d'Orsay, Université Paris-Saclay, 91405 Orsay Cedex, France

<sup>9</sup>CMAP, CNRS, École Polytechnique, Institut Polytechnique de Paris, 91128 Palaiseau Cedex

<sup>10</sup>Laboratoire d'Analyse Mathématiques Appliquées, CNRS UMR 8050, Université Gustave Eiffel (UPEC), F-77454, Marne-la-Vallée, France



(Received 27 October 2022; accepted 20 September 2023; published 6 November 2023)

Granular flows occur in various contexts, including laboratory experiments, industrial processes, and natural geophysical flows. To investigate their dynamics, different kinds of physically based models have been developed. These models can be characterized by the length scale at which dynamic processes are described. Discrete models use a microscopic scale to individually model each grain, Navier-Stokes models use a mesoscopic scale to consider elementary volumes of grains, and thin-layer models use a macroscopic scale to model the dynamics of elementary columns of fluids. In each case, the derivation of the associated equations is well-known. However, few studies focus on the extent to which these modeling solutions yield mutually coherent results. In this article, we compare the simulations of a granular dam break on a horizontal or inclined planes for the discrete model convex optimization contact dynamics (COCD), the Navier-Stokes model Basilisk, and the thin-layer depth-averaged model SHALTOP. We show that, although all three models allow reproducing the temporal evolution of the free surface in the horizontal case (except for SHALTOP at the initiation), the modeled flow dynamics are significantly different, and, in particular, during the stopping phase. The stresses measured at the flow's bottom, reflecting the flow dynamics, are in relatively good agreement, but significant variations are obtained with the COCD model due to complex and fast-varying granular lattices. Similar conclusions are drawn using the same rheological parameters to model a granular dam break on an inclined plane. This comparison exercise is essential for assessing the limits and uncertainties of granular flow modeling.

DOI: [10.1103/PhysRevE.108.054902](https://doi.org/10.1103/PhysRevE.108.054902)

### I. INTRODUCTION

Dry granular flows have been widely studied over the past decades, from industrial processes [1,2] to geophysical flows such as rockfalls [3–5], rock and debris avalanches [6–8], pyroclastic flows [9,10], or, more generally, dry landslides both on Earth and other planets [11,12].

Laboratory experiments allow investigating the physical processes controlling granular flow dynamics, such as self-channeling [13–15], particle size segregation [2], and bed erosion [16–18]. Nevertheless, some key flow characteristics are challenging to measure in experiments but can be directly estimated in numerical simulations, like the pressure inside the flow or the velocity field. Numerical modeling also helps to validate physically based models used to describe the processes at stake [4,19–21] to investigate configurations difficult

to set up in a laboratory, and flows at a larger scale such as at the field scale for geophysical flows, where topography effects play a major role. At the scale of landslides, one way to obtain information about their temporal behavior is through the inversion of the low-frequency seismic waves they generate. This inversion can then be used to reconstruct the history of forces (stress) exerted by the landslide on the ground.

Multiple modeling solutions exist depending on the scale of the flow description, rheological laws, and numerical methods. At the microscopic scale, simulations with discrete models, generally referred to as Discrete Element Methods (DEM), represent the granular flow by many distinct particles, and all grain-to-grain interactions are modeled [22–25]. This approach is supposedly the most realistic but has a high computational cost as the number of particles increases [e.g., [26–28]]. It limits their applicability to flows at larger scales. Furthermore, the large range of particle sizes that change in time due to fragmentation is still poorly handled despite the strong effect of particle segregation in granular flows

\*martin\_hugo@ymail.com

[4,29]. A second modeling solution considers the granular flow as a continuous medium and solves the Navier-Stokes equations to model the dynamics of each elementary volume, e.g., Refs. [30–33]. In this case, larger events can be modeled but the main difficulty remains in the definition of suitable rheological laws. Furthermore, simulating natural flows over complex topography still requires huge computational cost, which complexifies sensitivity analyses [34]. A third modeling option is based on the thin-layer approximation where the flow's thickness is assumed to be small compared to its extent, velocity is assumed to be parallel to the slope, and the equations are generally depth-averaged. Consequently, the model only solves for the thickness of the flow and its depth-averaged velocity. These models are often used empirically because the rheological parameters are calibrated to reproduce experiments or field observations [12]. However, thanks to their relatively low computational cost, they can be used at field scale to reproduce real geophysical events on complex topographies. Since the pioneering work of Refs. [35–37], they have been widely used for physics-based landslide hazard assessment [38–41]. Note that unlike the first option using discrete models, the continuous formulation of the Navier-Stokes and thin-layer models cannot represent blocking effects between particles or high-frequency fluctuations related to grain-grain and grain-bottom collisions.

All these models are classically tested by comparing observed and simulated granular flow travel distance (or runout) and deposits extent and thickness. Indeed, these characteristics are the easiest to observe on the field for geophysical flows. However, over the past decades, seismic waves generated by these flows have been increasingly used to constrain their dynamics (both at the laboratory and field scales, e.g. Refs. [42–45]). In turn, seismic waves can be used to calibrate both thin-layer models [46–49] and discrete models [50,51]. This is done, in particular, by comparing the basal force inverted from seismic signals and deduced from simulations (e.g., Refs. [49,51]). Thus, to accurately interpret the comparison between simulations and observations and be aware of their limitations, it is essential to understand how the dynamics of the simulated flow depends on the type of simulation tool.

Here, we present the differences that exist between simulations performed with these three models in the case of a granular dam break. Each model has its own pros and cons, depending on the scale of the flow and the objective of the simulation (e.g., laboratory-scale versus natural geophysical scale simulations). In this article, our aim is to highlight the similarities and differences, with a focus on their abilities to simulate mass profiles, flow dynamics, and basal stresses, and a systematic comparison between discrete, Navier-Stokes, thin-layer models, simultaneously with experimental data.

We then compare our 2D simulations, keeping, when possible, as a common reference the experiments (performed under 3D experimental conditions) of Farin *et al.* (2014) [17]. We investigate the discrepancies between discrete Navier-Stokes and thin-layer models, with three numerical codes: the discrete model convex optimization contact dynamics (COCD) [52], the Navier-Stokes model Basilisk [53], and the thin-layer model SHALTOP [20,54–57]. To allow for a more straightforward interpretation, we consider the simple case of

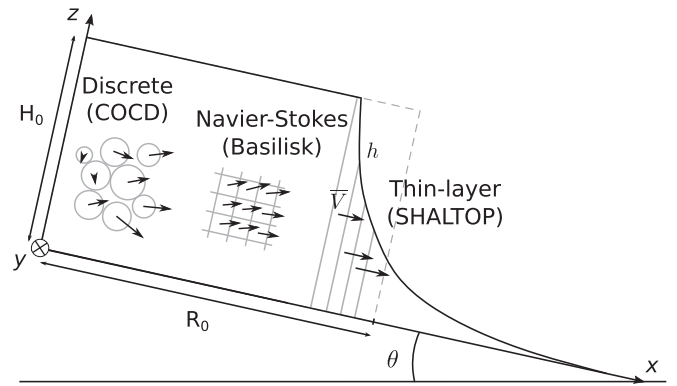


FIG. 1. Three different types of models to simulate granular dam break. Black arrows represent velocity vectors. In the discrete model (COCD), every disk has its own velocity; in the Navier-Stokes model (Basilisk), the velocity is defined in each cell while in the thin-layer model (SHALTOP), a depth-averaged velocity, parallel to the bed, is associated to each column. The dashed gray line represents the contour of the initial rectangular mass released from rest at  $t = 0$  s.

a 2D granular dam break, reproducing the 3D experiments of Ref. [17] for three slope angles  $\theta = 0^\circ, 10^\circ,$  and  $16^\circ$ . Rheological parameters are chosen to match the profiles of one dam break experiment. We compare these methods on their profiles evolution, deposits, dynamics, and normal stresses on the ground. In Sec. II, we present the experimental data used to calibrate the model. Then, in Sec. III, we describe the three different numerical models. Simulation results are presented in Sec. IV, then simulations of flow dynamics and basal normal stresses are discussed in Sec. V. An additional spectral analysis of COCD normal stress is done in the same section, with a discussion on rheological parameters; see Sec. V.

## II. EXPERIMENTAL SETUP

The experimental setup used in the simulations is sketched in Fig. 1 and fully described in detail in Farin *et al.* (2014) [17]. It consists of a 3-m-long channel of width 20 cm and inclination  $\theta$  between  $0^\circ$  and  $30^\circ$ . Let us define a Cartesian reference frame  $(x, y, z)$  linked to the bed, such that the  $z$  axis is perpendicular to the bed and the  $x$  axis is pointing in the downslope direction. In this reference frame, the channel base is given by  $z = 0$  (see Fig. 1).

The granular material consists of spherical glass beads released from rest as a rectangular mass of height  $H_0 = 14$  cm and length  $R_0 = 20$  cm. The corresponding aspect ratio is  $a = H_0/R_0 = 0.7$  and additional results with  $a = 0.31$  and  $1.24$  are available in Appendix E. The mean diameter of beads is  $d = 0.7 \pm 0.07$  mm. A layer of glass beads is glued to the plane. The initial mass is released by opening a gate in the direction perpendicular to the channel bed.

The experimental setups reproduced in our simulations correspond to slope angles  $\theta = 0^\circ$  and  $\theta = 16^\circ$ .  $\theta = 10^\circ$  and  $\theta = 22^\circ$  are also considered for comparison. The manner in which the initial state is constructed in simulations is described in detail in Appendix A. A snapshot of the initial state is depicted in Appendix E (Fig. 13).

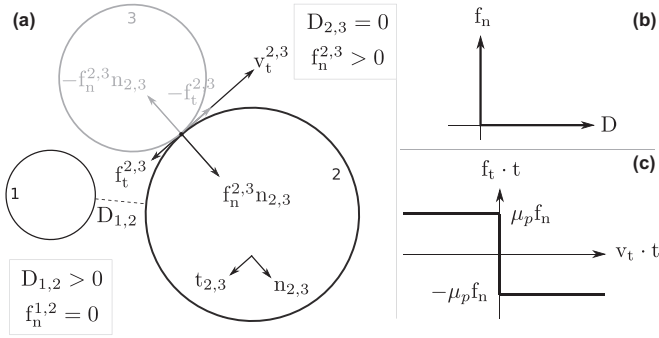


FIG. 2. Schematic representation of the two contact laws. (a) Notations for a three-disk situation: Disks 1 and 2 are not in contact, while disks 2 and 3 are.  $D_{i,j}$  ( $1 \leq i < j \leq 3$ ) represents the normal distance between disks  $i$  and  $j$ ,  $f_n^{i,j}$  is the intensity of the normal force at the contact,  $\mathbf{n}_{2,3}$  (respectively,  $\mathbf{t}_{2,3}$ ) is the unit normal (respectively, tangential) vector at the contact between 2 and 3,  $\mathbf{f}_t^{2,3}$  represents the tangential force vector, and  $\mathbf{v}_t^{2,3}$  is the tangential relative velocity vector between disks 2 and 3. (b) Graph of the normal law. (c) Graph of the Coulomb friction law.  $x \cdot y$  represents the dot product of two vectors  $x, y$ .

### III. NUMERICAL MODELS

The general concepts and equations of the different models used in this article are now briefly presented. More details on the simulation setups and output processing are given in Appendixes A and B. The values of the numerical parameters are given in Table I, Appendix D. The flow dynamics is solved on a 2D domain only. Interactions between the beads and lateral walls are thus not taken into account explicitly. The initial granular column is released from rest without accounting for the gate's initial lifting (see Ref. [31] for the effects of the gate).

#### A. The discrete model COCD

In discrete models, the granular mass is represented by a collection of rigid particles (see Fig. 1) like glass discs (or spheres in 3D). The motion equations are solved at each time step for all of these particles, determining their contact forces. Their interactions can be classically modeled through the Hertz theory, using nonlinear damp springs, as done in the molecular dynamics (MD) approach (see the seminal work of Cundall and Strack [22]). In this article, we use another approach named contact dynamics (CD), introduced by Moreau and Jean in the 1990s [23,58–62]. Unlike MD, where the contact forces are modeled by functions obtained from Hertz theory, in CD the forces are linear impulses, submitted to contact laws describing normal repulsion and tangential friction that are included in Newton's second law of motion.

Numerous numerical methods have been proposed for CD models [24,26,52,63–68]. Classically, one shall specify the normal and tangential contact laws, which must be verified for every contact and time step (Fig. 2). The normal law is based on a nonoverlapping constraint, a complementary relation between the normal distance and the intensity of the normal contact force [Fig. 2(b)]. It means that grains cannot overlap or interact if they are not in contact, and the force

between two grains is always repulsive, i.e.,

$$0 \leq D^\alpha, \quad f_n^\alpha D^\alpha = 0, \quad f_n^\alpha \geq 0, \quad (1)$$

where  $\alpha$  is the number associated to a contact between two particles,  $D^\alpha$  is the normal distance that measures the gap between the two particles, and  $f_n^\alpha$  is the normal force intensity between them. These relations are supplemented by the inelastic contact law. The tangential contact law that is verified for all contacts is the Coulomb friction law [Fig. 2(c)], involving the tangential and normal components of the contact force belonging to Coulomb's cone, i.e.,

$$\begin{aligned} \mathbf{f}_t^\alpha &= -\mu_p f_n^\alpha \mathbf{v}_t^\alpha / \|\mathbf{v}_t^\alpha\|, & \text{if } \|\mathbf{v}_t^\alpha\| > 0, \\ \|\mathbf{f}_t^\alpha\| &\leq \mu_p f_n^\alpha, & \text{if } \|\mathbf{v}_t^\alpha\| = 0, \end{aligned} \quad (2)$$

where  $\mu_p$  is the friction coefficient between the particles,  $\mathbf{f}_t^\alpha$  is the tangential force vector, and  $\mathbf{v}_t^\alpha$  is the tangential relative velocity vector between the two particles involved in the contact  $\alpha$ .

In this article, to compute the approximated solution of the motion equation including contact laws (1) and (2), we use the numerical method COCD, described in Ref. [52]. In this particular approach, the numerical scheme is a natural discretization of Newton's second law and the nonoverlapping constraint (1) is convexified. Doing so, the grains' velocities and positions may be computed simultaneously using an implicit scheme, which requires solving a convex minimization problem with conic constraints at each time step.

The mechanical behavior of such discrete media results from a combination of geometrical rearrangements between particles and interparticle friction forces. In our discrete model, the only rheological parameter is the interparticle friction coefficient  $\mu_p$ , present in the tangential law (2), and which is calibrated to reproduce laboratory experiments. More precisely, the macroscopic static friction coefficient  $\mu_s = \tan(\theta_m)$ —where  $\theta_m$  is the static friction angle, i.e., the angle that the granular mass forms at rest—can be interpreted as the combination of the interparticle friction coefficient  $\mu_p$  and the geometric trapping (dilatancy effect)  $\mu_g$  [69]. The coefficient  $\mu_g$  is linked to the grains' shapes, masses, or inertia, while  $\mu_p$  is a given parameter of the model, and used in the classical Coulomb's law of friction at any grain-grain or grain-wall contact [52].

In this article, 2D simulations only are considered for comparing the three models. The value for  $\mu_p$  used here is derived from back analysis by reproducing the deposits from experiments through 2D simulations in the horizontal case. The best-fit interparticle friction coefficient is  $\mu_p = 0.9$ . Note that this value is relatively large compared to the friction coefficient  $\mu_p = 0.3$ , calibrated by comparing 3D simulations and experiments [52], and which is in the range of friction coefficients measured for a perfect glass-glass contact  $\mu_p = 0.4$  [70], and that measured with MD  $\mu_p = 0.16$  [71]. In COCD, this difference in calibrated friction coefficients arises when comparing mass profiles in 2D and 3D simulations. We discuss this point in Sec. VE.

### B. Basilisk

Basilisk [53] is a continuum multiphase flow solver based on a finite volume method (see Fig. 1) and volume-of-fluid approach to track the interface between phases. In our case, these two phases are air and granular phase. The Eulerian mesh grid remains constant in the granular material and coarsens in the air (see Fig. 2 of Ref. [72] for an illustration). Basilisk solves the local incompressible mass and momentum equations:

$$\nabla \cdot \mathbf{V} = 0, \quad (3)$$

$$\rho \left( \frac{\partial \mathbf{V}}{\partial t} + \mathbf{V} \cdot \nabla \mathbf{V} \right) = \rho \mathbf{g} - \nabla p + \nabla \cdot (2\eta D), \quad (4)$$

where  $\mathbf{V} = (V_x(x, z, t), V_z(x, z, t))$  is the velocity field with components  $V_x$  and  $V_z$  in the  $x$  and  $z$  directions, respectively,  $\mathbf{g}$  is the gravity field,  $\rho$  is the density, and  $\eta$  the dynamic viscosity. This is equivalent to writing the stress tensor  $\sigma$  as

$$\sigma = -pI_d + \sigma', \quad (5)$$

$$\sigma' = 2\eta D, \quad (6)$$

where  $\sigma'$  is the deviatoric stress tensor,  $I_d$  is the identity tensor, and the strain rate tensor is

$$D = \frac{1}{2}(\nabla \mathbf{V} + \nabla \mathbf{V}^t). \quad (7)$$

Basilisk thus solves the velocity field and the pressure in the granular phase provided a constant value or a rheological law is given to define  $\eta$ .

The  $\mu(I)$  rheology has met with growing success to model granular flows [73,74]. When considering simple shear dry granular flows, dimensional arguments and numerical simulations showed that the shear stress is proportional to the pressure  $p$ , through a coefficient  $\mu$  that depends on the inertial number  $I$ . The tensor formulation of this rheology is [74]

$$\sigma' = \frac{\mu(I)p}{\|D\|} D, \quad (8)$$

$$\text{with } I = \frac{2\|D\|d}{\sqrt{p/\rho}}, \quad (9)$$

with  $\|D\| = \sqrt{0.5D_{ij}D_{ij}}$  and  $d$  the mean diameter of grains belonging to the granular phase. Thus, the  $\mu(I)$  rheology boils down to considering a viscous fluid, with a nonconstant viscosity  $\eta$ :

$$\eta = \frac{\mu(I)p}{2\|D\|}. \quad (10)$$

Finding an explicit and general relation between the coefficient  $\mu$  and the inertial number  $I$  is an open question. The most common expression of  $\mu(I)$  derived for steady flows on constant slopes is given by

$$\mu(I) = \mu_1 + \frac{\mu_2 - \mu_1}{1 + I_0/I}, \quad (11)$$

where  $\mu_1$ ,  $\mu_2$ , and  $I_0$  are constants. But the resulting model may be ill-posed: small-scale instabilities in the flow can significantly affect simulations results [32,75]. Nevertheless, we use this expression. Furthermore, to avoid numerical divergence when  $\|D\|$  tends to 0 in Eq. (10), a maximum value for the viscosity  $\eta_{\max} = 24000 \text{ Pa s}$  is imposed following

Ref. [30] to regularize the problem when the strain rate tends to zero.

The friction coefficients are  $\mu_1 = 0.48$ ,  $\mu_2 = 0.73$ , and  $I_0 = 0.279$ . Solving the same equations, they have been calibrated for  $a = 0.7$  and  $\theta = 0^\circ$  through an augmented Lagrangian method and were quantitatively compared to granular collapse experiments [31]. Note that these rheological parameters have been slightly overestimated compared to experimental measurements [74]. The calibration of the model on experiments requires higher friction coefficients than those including wall effects since Martin *et al.* (2017) [32] added in some ways two times wall effects. For a detailed analysis of the wall effects in Navier-Stokes and thin-layer models, see Refs. [32,76], respectively. A discussion about the influence of the rheological parameters is presented in Sec. V.

### C. SHALTOP

Depth-averaged thin-layer granular flow simulations are carried out with the SHALTOP numerical code [20,54–57]. This code has been successfully used to simulate both laboratory experiments [56] and field scale landslides on Earth and other planetary bodies, e.g., Refs. [8,12,46,77,78]. SHALTOP also proved to accurately reproduce analytical solutions of the dam-break problem [79–81] and was compared to other depth-averaged models in one of the only benchmark exercise for these types of codes [82].

To match as closely as possible the equations implemented in Basilisk, we use a depth-averaged version of the  $\mu(I)$  rheology following [19,20,83]. Considering  $h$ , the mass height and  $\bar{V}$ , the depth-averaged downslope velocity (see Fig. 1), the resulting mass and momentum equations are

$$\frac{\partial h}{\partial t} + \frac{\partial (h\bar{V})}{\partial x} = 0, \quad (12)$$

$$\frac{\partial (h\bar{V})}{\partial t} + \frac{\partial (h\bar{V}^2)}{\partial x} = S_1, \quad (13)$$

with

$$S_1 = gh \cos(\theta) \left( \tan(\theta) - \frac{\partial h}{\partial x} \right) - gh \cos(\theta) \mu(I) \frac{\bar{V}}{|\bar{V}|}. \quad (14)$$

The term  $S_1$  includes the gravitational and longitudinal pressure forces, and a bottom friction force where  $\mu(I)$  appears. As for Basilisk,  $\mu(I)$  is given by Eq. (11), but with the depth-integrated version of the inertial number  $I$ ,

$$I = \frac{5d\bar{V}}{2h\sqrt{gh}\Phi \cos(\theta)}, \quad (15)$$

where  $\Phi$  is the volumetric solid fraction.

Note that in the derivation of the corresponding thin-layer equations for flows on inclined planes given in Refs. [83,84], an additional viscous term  $S_2$  appears on the right-hand side of Eq. (13),

$$S_2 = \frac{\partial}{\partial x} \left( \nu h^{3/2} \frac{\partial \bar{V}}{\partial x} \right), \quad (16)$$

where  $\nu$  is a coefficient that can be related to bed slope, while  $\mu_1$  and  $\mu_2$  are rheological parameters (see Eqs. (4.16) in Ref. [84]). However, the expression of  $\nu$  in Ref. [84] is valid

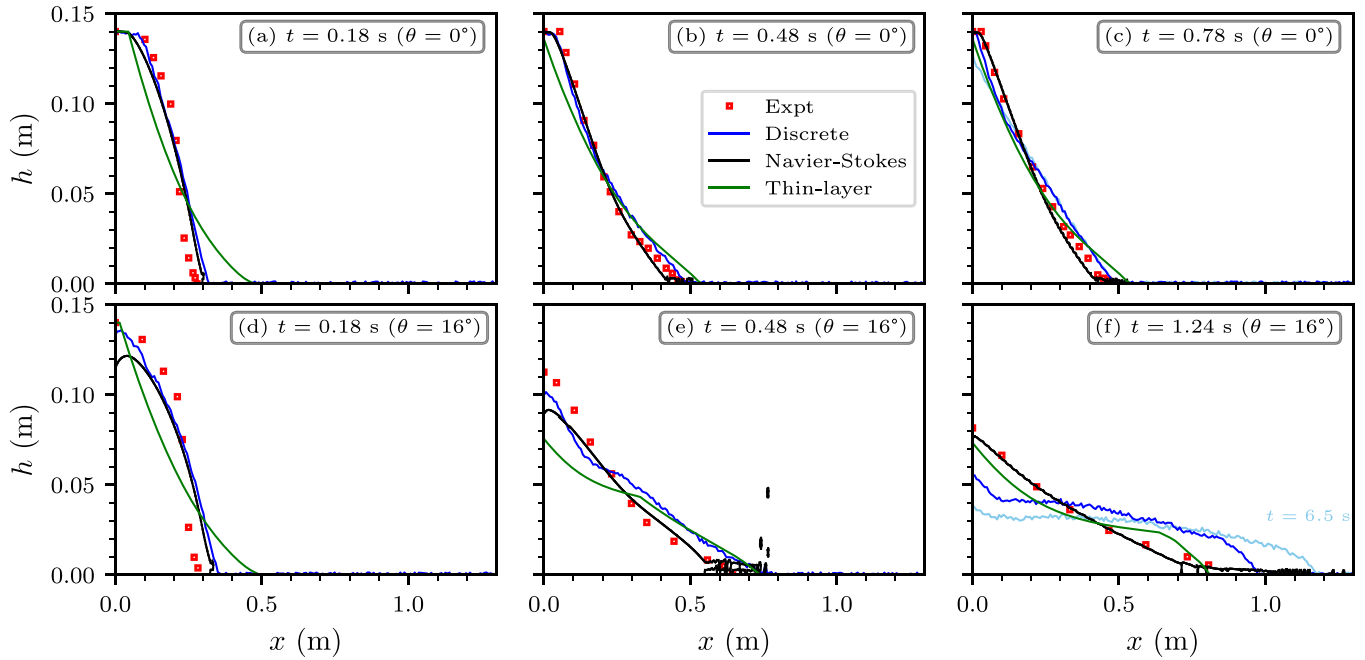


FIG. 3. Comparison between experiments and numerical simulations of the granular profiles during a dam break. We display the experimental results (red squares), discrete COCD simulations (blue line), Navier-Stokes Basilisk simulations (black line), and thin-layer SHALTOP simulations (green line). The initial aspect ratio is  $a = 0.7$ , with a bed slope  $\theta = 0^\circ$  (a)–(c) and  $\theta = 16^\circ$  (d)–(f). The light blue line in (c) and (f) is the discrete simulation profile at  $t = 6.5$  s.

for steady flows only, when  $\mu_1 < \tan(\theta) < \mu_2$ , which is not the case in our simulations. More generally, it is not valid for complex, non planar topographies. As we want our results to help improve the interpretation of thin-layer simulations at the field scale, we will thus not consider the viscous term  $S_2$  in our simulations. In addition, comparisons with experiments in Sec. IV A show that the depth-averaged  $\mu(I)$  rheology without viscosity already allows us to correctly match granular collapse deposits.

We use the same rheological parameters as for Basilisk simulations:  $\mu_1 = 0.48$ ,  $\mu_2 = 0.73$ , and  $I_0 = 0.279$ . For simplicity, the solid fraction in Eq. (15) is set to  $\Phi = 1$ , as it allows us to match mass profiles observed in experiments and simulated with Basilisk, both for  $\theta = 0^\circ$  and  $\theta = 16^\circ$ . We tested  $\Phi = 0.6$ , and results are very similar to  $\Phi = 1$ . Thus, in thin-layer simulations, the main controlling parameters are the friction coefficients  $\mu_1$  and  $\mu_2$ , and not the volume fraction  $\Phi$ . We investigated the sensitivity of the results to  $\mu_1$  and  $\mu_2$  in Sec. V D.

## IV. RESULTS

To compare the discrete Navier-Stokes and thin-layer models together, and with laboratory experiments, we focus on the spatiotemporal change of the flow thickness  $h(x, t)$ , the position of the flow front  $x_f(t)$ , the velocity field, and the arrest phase, as well as on the basal normal stress  $\sigma_b$  and the hydrostatic pressure  $p_h$ , both applied by the flow to the bed. Appendix B details how all these quantities are computed in the different models, and Table I in Appendix D gives all numerical parameters.

## A. Granular mass profiles

### 1. Horizontal plane

The first row of Fig. 3 shows comparisons between experimental measurements of the granular mass profile on a horizontal plane ( $\theta = 0^\circ$ ) and the different numerical models at three different times. After the column release at  $t = 0$  s, the mass spreads on the plane, decelerates, and stops to form a deposit. The mass profiles obtained with the Navier-Stokes model Basilisk reproduce very well the overall granular spreading (compare black line and red squares in Fig. 3). Moreover, the final deposit is in excellent agreement with the experiment, although the initial spreading is slightly faster in the simulation [Fig. 3(a)].

The profiles resulting from the discrete model are initially very similar to those obtained using the Navier-Stokes model. However, the final deposit slightly differs from the experiment, with a concave shape of the frontal part while the deposit front is slightly convex [Figs. 3(c) and 3(f)].

The depth-averaged thin-layer model SHALTOP overestimates the initial spreading. However, despite the initial overestimation of the velocity, the final deposit is in good agreement with the experiments with a run-out distance overestimated by less than 15%.

### 2. Inclined plane

The second row of Fig. 3 shows similar profiles of the granular mass on an inclined plane  $\theta = 16^\circ$ , simulated with the same rheological parameters as for the horizontal plane. In this case, the results are more sensitive to the numerical model used. The thin-layer model SHALTOP is faster than the others but yields a final deposit in good agreement with the

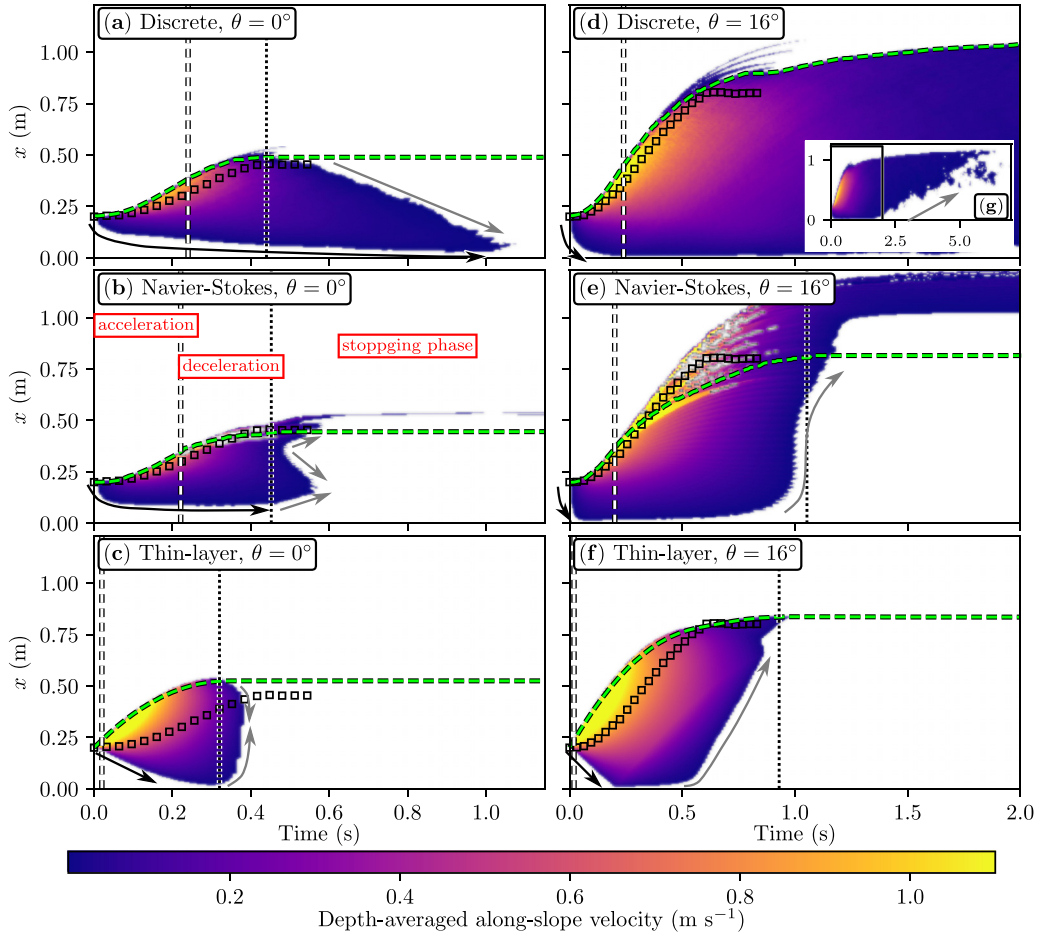


FIG. 4. Spatiotemporal plot representing the depth-averaged along-slope flow velocity  $\bar{V}_x(x, t)$  (color scale) for the different models, with  $\theta = 0^\circ$  (a)–(c) and  $\theta = 16^\circ$  (d)–(f). We only display velocities above  $1 \text{ cm s}^{-1}$  (lower velocities are represented in white), as in the experiments of Ref. [17]. For each simulation, the green dashed line represents the time evolution of the front position. The acceleration and deceleration phases are separated by a vertical white dashed line, and the deceleration and stopping phases by a vertical black dotted line. Black arrows follow the rarefaction wave where the mass initially at rest is set in motion. Grey arrows follow the stopping wave where the moving mass stops. Black squares give the front position in experiments.

experiment. The mass profile has a concave and rounded front compared to the thin experimental front, and the thickness at the rear of the flow decreases faster.

The Navier-Stokes model Basilisk is in good agreement with the experiments throughout the collapse although, the flow being faster than on the horizontal case, some drops and bubbles appear at the front as numerical artifacts (see Sec. V A). At  $t = 1.24 \text{ s}$ , a thin layer (lower than  $3.5 \text{ mm}$ ) develops, which is not observed in the experiments. The overall profile is also slightly less convex than in the experiment, and the upper left thickness of the flow is decreasing faster as in the thin-layer model.

The most significant difference with the experiment is observed for the discrete model COCD, where the flow is still moving after  $1.24 \text{ s}$  (compare blue and pale blue lines in Fig. 3(f), giving the flow thickness at  $t = 1.24 \text{ s}$  and  $t = 6.5 \text{ s}$ , respectively). This difficulty in stopping the granular flow for  $\theta = 16^\circ$  is discussed in Sec. V.

Simulations for aspect ratios  $a = 0.31$  and  $a = 1.24$  have also been performed to check the accuracy of the models for various column collapses. Comparison of the free-surface

profiles are presented in Figs. 14 and 15 in Appendix E. Changing the aspect ratio of the initial column does not significantly change the overall behaviours observed for  $a = 0.7$ .

## B. Flow dynamics

We define the flow's front position  $x_f(t)$  as the maximal length reached by the flow, thicker than five-grain-diameters height in experiments, i.e.,  $h(x_f) \geq 5d = 3.5 \text{ mm}$ . The front position is represented for each simulation by a green dashed line in Fig. 4. The left position of the mass is always located at  $x = 0$ , whatever the time. The way the front is computed is explained in Appendix B. The colors in Fig. 4 represent the depth-averaged downslope velocity  $\bar{V}_x(x, t)$  and its space-time evolution at  $\theta = 0^\circ$  [Figs. 4(a)–4(c)] and  $\theta = 16^\circ$  [Figs. 4(d)–4(f)]. The velocities represented in white are those smaller than the cutoff velocity  $1 \text{ cm s}^{-1}$ , set as in Ref. [17]. It highlights the spatiotemporal characteristics of the stopping phase.

To describe the dynamics of the dam break, we define three different phases. First, the *acceleration phase* starts when

the gate is instantaneously removed and ends when the front reaches its maximal velocity. The *deceleration phase* follows, and we arbitrarily define its end when the front stops, even if the rest of the mass may still be flowing. Finally, the *stopping phase* follows and ends when all the material is at rest. The end of the acceleration (respectively, deceleration) phase is represented by a vertical white dashed line (respectively, dotted black line) in Fig. 4.

The transitions between the static and moving states within the granular mass are given by black and gray arrows in Fig. 4. The black arrow corresponds to a rarefaction wave propagating from the front to the back of the flow, initiating the movement of materials initially at rest. On the contrary, the grey arrow corresponds to stopping waves, when materials in movement come to rest. This stopping wave can be initiated at the front of the flow towards the back [Fig. 4(a)], from the back towards the front [Fig. 4(f)], or from any location within the mass towards the front or the back [Fig. 4(b)].

### 1. Acceleration phase

Figures 4(a)–4(c) at  $\theta = 0^\circ$  show a significant difference between the thin-layer and the two other models in the acceleration phase of the granular mass. This phase is very fast, if not instantaneous, in the thin-layer model: less than 0.02 s, when simulations outputs are written every 0.01 s. It is more progressive in the discrete (0.24 s) and Navier-Stokes (0.22 s) models, in better agreement with experiments (black squares). The propagation of the static (flowing) interface (transition between violet and white colors along the black arrows in Fig. 4) towards the left of the column in the thin-layer model is also different from the other models [Figs. 4(a)–4(c)]. Indeed, this interface propagates with an almost constant velocity in the thin-layer model while, in the discrete and Navier-Stokes models, it propagates with decreasing velocity. In the Navier-Stokes model, the static (flowing) interface stays almost at the same position  $x = 0.12$  m for  $t > 0.1$  s [Fig. 4(b)].

The lighter colors in Fig. 4(c) compared to Figs. 4(a) and 4(b) show that the maximum depth-averaged velocity  $\bar{V}$  in the thin-layer model is always higher than in the other models (above  $1.1$  m s<sup>-1</sup>). We discuss this result in detail in Sec. V A 1.

For a dam break on the inclined plane  $\theta = 16^\circ$ , Figs. 4(d)–4(f) show qualitatively the same behavior during the acceleration phase as on the horizontal plane. Although velocities are higher, acceleration durations are similar to the horizontal slope case (instantaneous for SHALTOP, 0.24 s for COCD and 0.20 s for Basilisk). In comparison, in the experiments, the acceleration phase lasts 0.26 s and 0.29 s for  $\theta = 0^\circ$  and  $\theta = 16^\circ$ , respectively.

### 2. Deceleration phase

On a flat bottom [Figs. 4(a)–4(c)], the deceleration phases have a similar duration in the discrete COCD and Navier-Stokes Basilisk simulations (about 0.2 s, between white dashed and black dotted lines in Figs. 4(a) and 4(b)). The portion of the initial mass that does not move on the left is slightly larger with the Navier-Stokes model ( $x \leq 0.12$  m compared to  $x \leq 0.085$  m for the discrete model).

In the thin-layer model SHALTOP, the maximum velocities are higher (above  $1$  m s<sup>-1</sup>, compared to less than  $0.7$  m s<sup>-1</sup> in the other models), as expected. As the acceleration phase is instantaneous, the deceleration phase lasts the whole flow duration and ends at  $t = 0.32$  s. It is sooner than the Navier-Stokes and discrete models [0.45 s for both, black dotted lines in Figs. 4(a)–4(c)]. Finally, the motion still propagates backward throughout the deceleration phase in the thin-layer simulations, while the static (flowing) transition almost stays at the same position in the discrete model and only slightly propagates backward in the Navier-Stokes model [compare black arrows in Figs. 4(a)–4(c)].

In the thin-layer simulation at  $\theta = 16^\circ$ , the static (flowing) transition (rarefaction wave) propagates towards the back during a shorter duration than in the horizontal bed case [compare black arrows of Figs. 4(c) and 4(f)], and reaches the rear of the initial mass after about 0.2 s [black arrow in Fig. 4(f)]. Between  $t = 0.2$  s and  $t = 0.6$  s, almost the whole mass is moving. Then, after  $t = 0.6$  s, the stopping wave [gray arrow in Fig. 4(f)] propagates at constant speed towards the flow's front.

A qualitatively similar but more complex behavior is observed in the Navier-Stokes model at  $\theta = 16^\circ$ , but at a later time [from  $t \simeq 0.7$  s, Fig. 4(e)]. The flow front is also more contaminated by drops and air bubbles than at  $\theta = 0^\circ$  due to increased flow front velocity [compare colors irregularities between Figs. 4(b) and 4(e)]. The stopping waves are initiated during the deceleration phase for  $\theta = 16^\circ$ , from the left wall and propagates faster than in thin-layer and discrete simulations (the flow almost stops at  $t = 1$  s).

There is no clear end to the deceleration phase (as defined in this article) for the discrete model at  $\theta = 16^\circ$  [Fig. 4(b)], since the flow is still slightly moving down the slope at  $t = 6.5$  s.

### 3. Stopping phase

On the horizontal bottom, the stopping phases are very different from one model to the other. The stopping phase simulated by the thin-layer model is very short, less than 0.1 s [Fig. 4(c)]. The granular mass stops from both the front and the rear in an almost symmetrical way [gray arrows in Fig. 4(c)]. The stopping phase simulated with the Navier-Stokes model lasts slightly longer (about 0.15 s) but displays three stopping waves: one from the rear towards the front and two from the middle of the flow propagating in opposite directions [Fig. 4(b)]. This is a direct consequence of the stopping criteria in the Navier-Stokes code Basilisk; see Sec. V A. In discrete simulations, the stopping phase is more extended (about 0.6 s), with only one stopping wave propagating from the front to the rear at almost constant velocity [about  $0.7$  m s<sup>-1</sup>, Fig. 4(a)].

On the inclined plane  $\theta = 16^\circ$ , the stopping phase is different from that observed at  $\theta = 0^\circ$ . This phase is almost nonexistent in the thin-layer simulations as the front is the last portion of the flow still in motion. Similar qualitative behavior is obtained with the Navier-Stokes model if we disregard the thin layer that stays in motion beyond the front [above the green dashed line in Fig. 4(e)]. Indeed, the mass never wholly stops in the Navier-Stokes code Basilisk in the inclined case

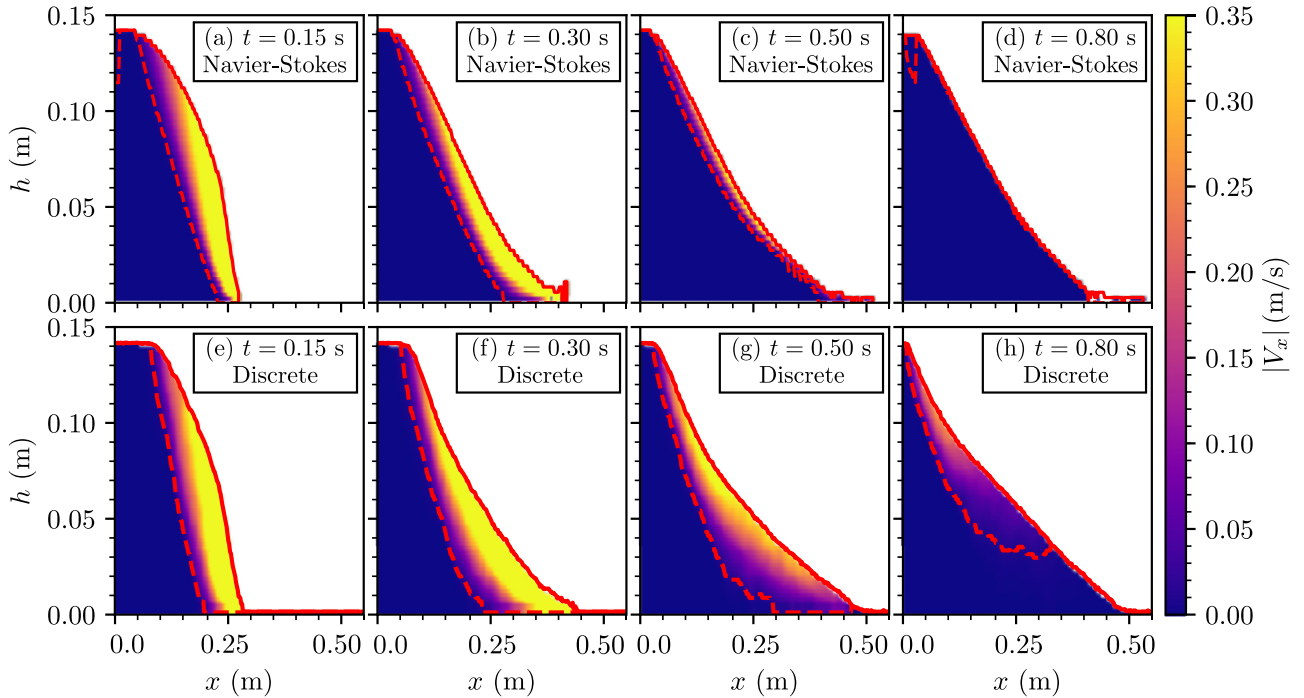


FIG. 5. Comparison between the horizontal velocity  $V_x$  calculated with the Navier-Stokes (Basilisk) (first row) and discrete (COCD) (second row) simulations, for  $\theta = 0^\circ$ . The red continuous line represents the free surface while the red dashed line the static (flowing) transition, considering a threshold value  $V_x = 1 \text{ cm s}^{-1}$ , as in Ref. [17]. (a), (e) belong to the acceleration phase; (b), (f) to the deceleration phase; and (c), (d), (g), (h) to the stopping phase.

(see Discussion in Sec. V A 3). The drops beyond the front that still move after 1. s are thin and slow and continue flowing until the end of the simulated time (here 1.24 s). In the discrete model, the stopping phase starts at  $t = 6 \text{ s}$  [Fig. 4(g)], and the mass never entirely stops during the calculation time, as continuous rearrangements keep occurring behind the front. This is not the case when smaller inclinations are considered (see Sec. V A).

In all simulations, the final front position is each time in good agreement with the final front position from experiments (compare black squares and green dashed lines in Fig. 4). For  $\theta = 0^\circ$ , the front stops at similar times in experiments, discrete and Navier-Stokes simulations (0.45 s), while the front stops sooner in thin-layer simulations (0.32 s). However, for  $\theta = 16^\circ$ , the front in the experiments stops at 0.64 s, but simulated fronts stop later: 0.93 s for the thin-layer model, 1.05 s for the Navier-Stokes model, and 6 s for the discrete model.

Despite the differences observed between the discrete and the Navier-Stokes models in their spatiotemporal representation of the depth-averaged velocity (Fig. 4), their resulting mass profiles are relatively in good agreement, especially for  $\theta = 0^\circ$  [see Figs. 3(a)–3(c)], meaning that different rheological processes may lead to the same granular profiles. This result is confirmed by comparing the two velocity fields and the static (flowing) interface as in Sec. IV B 4.

Other comparisons of the spatiotemporal evolution of the depth-averaged velocity profile are presented for  $a = 0.31$  (Fig. 16) and 1.24 (Fig. 17) in Appendix E, which show that changing the aspect ratio of the initial column does not significantly change the overall behaviours observed for  $a = 0.7$ .

#### 4. Velocity field and static (flowing) interface in discrete and Navier-Stokes models

The evolution of the horizontal velocity norm through the depth of the flow and during the collapse,  $|V_x(z, t)|$  is shown in Fig. 5 for  $\theta = 0^\circ$ . This information can only be obtained using the discrete and Navier-Stokes models since the velocity is depth-averaged in the thin-layer, one-layer model considered here. The static (flowing) transition is defined by considering a velocity threshold of  $1 \text{ cm s}^{-1}$ , as in the previous section and in Ref. [17].

Figures 5(a) and 5(e), corresponding to  $t = 0.15 \text{ s}$ , are snapshots of the velocity field during the acceleration phase for the Navier-Stokes and the discrete models. During this phase, the horizontal velocities obtained with the two models are similar (compare the colors). The static (flowing) interfaces also have a similar shape (red dashed line).

Figures 5(b) and 5(f), at  $t = 0.30 \text{ s}$ , correspond to the deceleration phase for both simulations (the flow front has started to slow down). Although velocities are comparable, the moving part inside the column is larger in the discrete simulation. In particular, the horizontal length of the flowing domain, behind the flow front, is 12 cm for the Navier-Stokes [Fig. 5(b)] and 20 cm for the discrete model [Fig. 5(f)].

We observe notable differences between the Navier-Stokes model [Figs. 5(c) and 5(d)] and the discrete model [Figs. 5(g) and 5(h)] during they stopping phase even though similar profiles of the deposit are obtained. The static (flowing) interface propagates from the front to the left and from the bottom to the free surface for the discrete code (see the evolution of the red dotted line between  $t = 0.5 \text{ s}$  and 0.8 s [Figs. 5(g) and



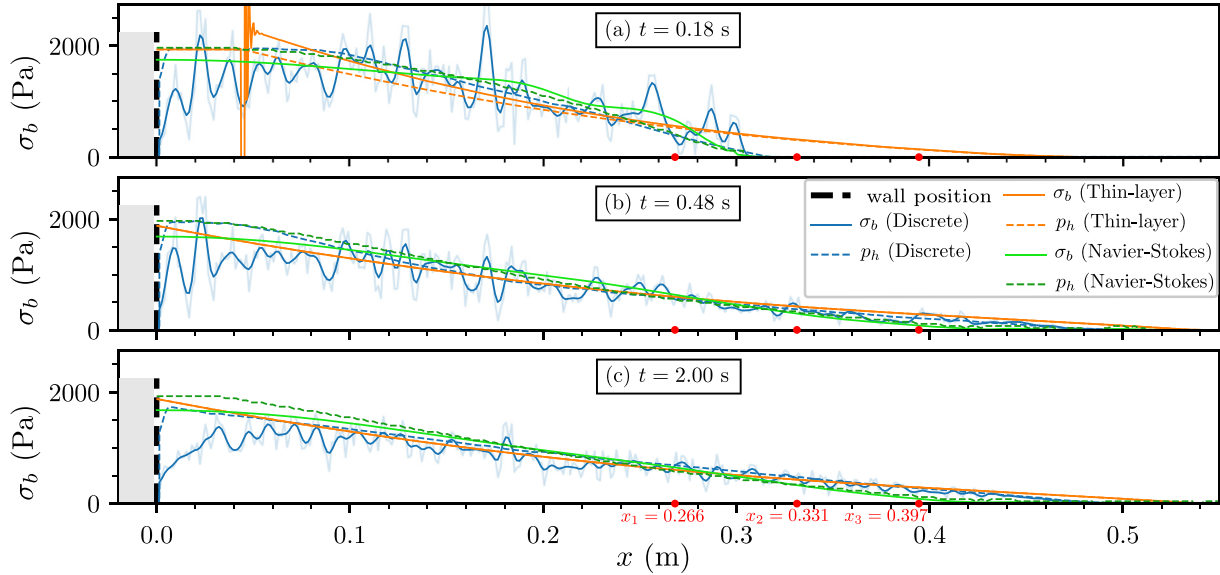


FIG. 6. Basal normal stress and hydrostatic pressure for  $\theta = 0^\circ$ . (a)  $t = 0.18$  s, (b)  $t = 0.48$  s, (c)  $t = 1.99$  s. For each simulation, we compute the basal normal stress  $\sigma_b$  and the hydrostatic pressure  $p_h$ . The light blue, respectively, dark blue, curve is the raw, respectively, smoothed, normal stress derived from discrete COCD simulations. See Appendix B 3 for details on computation. The gray light at the right of the wall limit (dashed black line) represents the left wall.

5(h)]. For the Navier-Stokes simulations, the front is always moving and the static (flowing) interface goes up uniformly from the bottom towards the free surface between  $t = 0.5$  and  $0.8$  s [Figs. 5(c) and 5(d)].

The discrete simulation shows deeper rearrangements than for the Navier-Stokes model, even after the flow front has stopped. Indeed, motion occurs 4 cm below the free surface at  $t = 0.5$  s with velocities locally higher than  $0.35 \text{ m s}^{-1}$  [Fig. 5(g)]. At  $t = 0.8$  s [Fig. 5(h)], velocities are below  $0.25 \text{ m s}^{-1}$ , but motion still occurs 3 cm below the surface. We can clearly identify in Fig. 5(h) the progression of the stopping wave that propagates from the flow front towards the rear.

**C. Basal stress**

**1. Spatial variations**

The basal normal stress  $\sigma_b$  and hydrostatic pressure  $p_h$  derived from the three codes are represented along with the domain in Fig. 6 for  $\theta = 0^\circ$ , at three different times:  $t = 0.18$  s,  $t = 0.48$  s, and  $t = 2.0$  s, where the flow is at rest in the three simulations [see the corresponding mass profiles at these times in Fig. 3(c)]. The basal stress  $\sigma_b$  is the stress applied to the bottom by the mass. It may differ from the hydrostatic pressure  $p_h$  related to the weight of the granular column on the bottom. The way  $\sigma_b$  and  $p_h$  are computed in each code is described in Appendix B 3.

The stresses  $\sigma_b$  and pressures  $p_h$  computed from the discrete and Navier-Stokes models are in good agreement for  $x \geq 0.2$  m [i.e., at the right of the initial gate, see Figs. 6(a)–6(c)] even though  $\sigma_b$  is much smoother in the Navier-Stokes model.

The thin-layer model compares well with the others except for  $t = 0.18$  s [Fig. 6(a)], where its front is too far (0.48 m in

the thin-layer model against 0.31 m for the others). As already mentioned in Sec. IV A, it is because the flow propagates faster in thin-layer models. The other difference is a perturbation observed at  $t = 0.18$  s and  $x = 0.045$  m in the stress  $\sigma_b$  (discussed in Sec. V B).

Significant variations in discrete simulation of  $\sigma_b$  are observed around the average values calculated in the other codes [compare blue line to other curves in Figs. 6(a)–6(c)]. These oscillations have amplitudes up to 75% of the mean value computed with the other codes at  $t = 0.18$  s, while they account only for 50% of it at  $t = 0.48$  s [Fig. 6(b)] and 20% at  $t = 2.0$  s [Fig. 6(c)], when the flow is at rest. These oscillations are expected in discrete models and are mainly due to the local structures formed by the contacts between grains, such as force chains, as well as grain-to-grain and grain-to-bottom impacts. Note that the more spatially smoothed the stress curve of the discrete model is, the closer it is to that of the other two models.

For  $x \leq 0.2$  m, we observe significant discrepancies between the different values of  $\sigma_b$  and  $p_h$ . For instance, the basal normal stress  $\sigma_b$  derived from discrete simulations is about 50% lower than the hydrostatic pressure  $p_h$  derived from the same simulation (compare blue plain lines and blue dashed lines in Fig. 6). Interestingly, Fig. 6 also shows that the stress applied on the bottom in the Navier-Stokes model can be different from the hydrostatic pressure. For instance, for  $x \simeq 0.15$  m at  $t = 0.18$  s, the basal normal stress is smaller than hydrostatic and, around  $x \simeq 0.15$  m, it gets higher; see Fig. 6(a). The Navier-Stokes normal stress  $\sigma_b$  also varies less in space, leading to smaller pressure gradients and thus smaller driving forces than those based on hydrostatic pressure in thin-layer models.

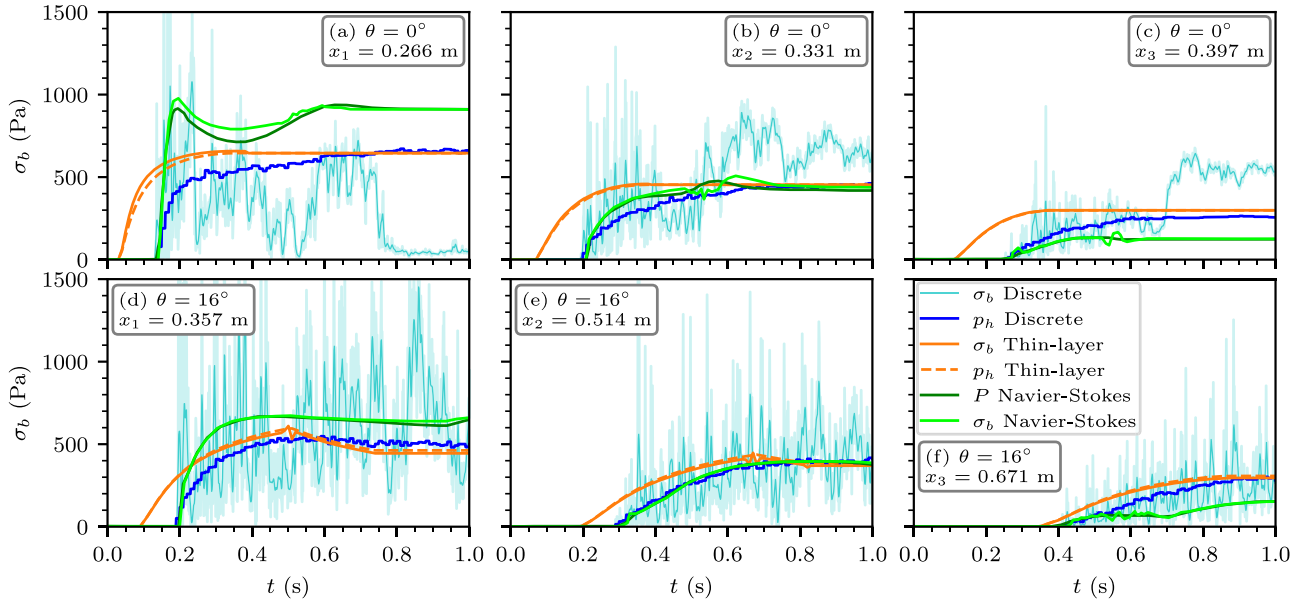


FIG. 7. Time evolution of basal normal stress  $\sigma_b$  (and hydrostatic pressure  $p_h$  for the discrete model) at three different probes, for  $\theta = 0^\circ$  [first row, (a)–(c)], and  $\theta = 16^\circ$  [second row, (d)–(f)]. For  $\theta = 0^\circ$  (respectively,  $16^\circ$ ), the probes positions are  $x_1 = 0.266$  m (a),  $x_2 = 0.331$  m (b), and  $x_3 = 0.397$  m (c) [respectively,  $x_1 = 0.357$  m (d),  $x_2 = 0.514$  m (e), and  $x_3 = 0.671$  m (f)]. These probes locations, respectively, correspond to 25%, 50%, and 75% of the distance between the run-out distance and the gate position ( $x = 0.2$  m). For discrete  $\sigma_b$ , the light blue, (respectively, dark blue) curve is the raw (respectively, smoothed), basal normal stress.

## 2. Temporal variation

We now proceed to compare the temporal fluctuations of basal stress at fixed positions. Understanding these variations is crucial to know if the seismic waves generated by the granular flow on the ground can be used to investigate the dynamics of the flow (e.g., Refs. [3,47,49,85]). In Fig. 7, we compare the temporal variation of stress  $\sigma_b$  and pressure  $p_h$  at three different locations (see caption of Fig. 7) for  $\theta = 0^\circ$  and  $\theta = 16^\circ$ . For each slope, the locations of probes  $x_1$ ,  $x_2$ , and  $x_3$  correspond, respectively, to 25%, 50%, and 75% of the run-out distance from the gate. For example, the probe locations are represented by red dots in Fig. 6(c). Figure 7 also shows the basal pressure, denoted  $P$ , for Navier-Stokes model Basilisk (khaki line), measured in the first cell above the bottom boundary layer.

The time at which the mass front reaches the probes is the minimal time with a nonzero stress signal. This time is shorter for thin-layer models than for the two others that are equal (Fig. 7). The difference is approximately 1 s for  $x_1$  and  $x_2$  [Figs. 7(a), 7(b), 7(d), and 7(e)] but can differ for  $x_3$  [Figs. 7(c) and 7(f)]. Another characteristic time is the duration needed by the mass to reach its local maximal height. It can be measured in Fig. 7 by the duration between the time where the front reaches the probe and the time at which the hydrostatic pressure is maximal. This duration is longer for thin-layer and Navier-Stokes models in the inclined case than for the horizontal plane. It is 0.06 s [Fig. 7(a)] against 0.2 s [Fig. 7(d)] for Navier-Stokes and 0.26 s [Fig. 7(a)] against 0.40 s [Fig. 7(d)]. While the discrete model is between them for  $\theta = 16^\circ$  (0.35 s [Fig. 7(d)]), it is much longer for the horizontal plane [0.75 s (Fig. 7(a))].

For  $\theta = 0^\circ$ , Fig. 7 shows that normal stress  $\sigma_b$  and pressure  $P$  are very close in the Navier-Stokes model, except for the

flow at high velocities [compare green and khaki lines for  $t \in [0.2, 0.4]$  s in Fig. 7(a)]. They are obviously equal when the mass is at rest,  $t \geq 2$  s [Figs. 7(a)–7(c)]. Additional stress variations appear in the Navier-Stokes model compared to the thin-layer model [see, e.g., Fig. 7(a)]. However, these variations are still much smaller and at much longer periods than the stress fluctuations calculated with the discrete model. At a given probe, the local stress computed by the discrete model can be completely different from the hydrostatic pressure [see  $\sigma_b$  for  $t \geq 0.8$  s in Figs. 7(a) and 7(c)].

The basal stresses simulated with the continuum models (thin-layer and Navier-Stokes) at  $\theta = 16^\circ$  are smaller than for  $\theta = 0^\circ$  for the same position to the front [compare Figs. 7(a) with 7(d), 7(b) with 7(e), and 7(d) with 7(f) (75%)]. Note that the instabilities of SHALTOP and Basilisk, already observed for  $\theta = 0^\circ$  and probe  $x_1$  [see Fig. 7(a)], are also visible for  $\theta = 16^\circ$  and probes  $x_1$ ,  $x_2$ , and  $x_3$  [see Figs. 7(d)–7(f)].

The behavior is more complex when looking at discrete simulations. Indeed, in that case, the basal stress fluctuations are much higher at  $\theta = 16^\circ$  than at  $\theta = 0^\circ$ . For the discrete model COCD, Figs. 7(b) and 7(d) clearly show that the basal stress can be almost two times higher or lower than the hydrostatic pressure. Indeed, in discrete simulations, when the mass is almost at rest for  $t \geq 0.8$  s,  $\sigma_b$  can be close to  $p_h$  [Figs. 7(d)–7(f)], lower than  $p_h$  [Fig. 7(a)], or higher than  $p_h$  [Figs. 7(b) and 7(c)].

## V. DISCUSSION

### A. Differences in flow dynamics

The discussion focuses here on the three different phases defined in Sec. IV B: the *acceleration*, the *deceleration*, and *stopping* phases.

**1. Flow initiation (acceleration phase)**

The flow initiation is quantitatively similar for the Navier-Stokes model Basilisk and the discrete model COCD (Figs. 3–5). During this initiation, the profiles obtained with the two codes slightly differ from the experiments from Ref. [17] [see Figs. 3(a) and 3(d)]. This may be due to the presence of a gate in experiments, where the release is fast but not instantaneous [31]. The thin-layer model SHALTOP overestimates the initial spreading with higher velocities than the others [compare Fig. 4(c) with Figs. 4(a) and 4(b), and Fig. 4(f) with Figs. 4(d) and 4(e)]. This well-known behavior of such models [56,76] is due to non-negligible vertical velocities (accelerations) leading to nonhydrostatic pressure inside the granular column, which contradicts the thin-layer approximation (e.g., Fig. 12 in Ref. [86]). Furthermore, the analytical solution of the dam-break problem, described by thin-layer equations with constant friction coefficient smaller than the tangent of the bed slope, shows that the front velocity in these models is maximum at  $t = 0$  s (see Ref. [79] and Eq. (3) in Ref. [16]). This is consistent with our simulations where the acceleration phase is less than 0.02 s (when outputs are written every 0.01 s), although in our case the friction coefficient is not constant and is higher than the slope bed.

These behaviors are qualitatively similar for  $\theta = 0^\circ$  and  $\theta = 16^\circ$ . The duration of the acceleration phases simulated by the discrete and Navier-Stokes models does not depend much on the slope (between 0.20 and 0.24 s for both  $\theta = 0^\circ$  and  $\theta = 16^\circ$ ). This is coherent with laboratory experiments (see location of the curves' maximums in Fig. 9(b) in Ref. [16]).

**2. Deceleration phase**

The deceleration phases are quantitatively similar for the Navier-Stokes and discrete models' COCD [Figs. 3(a), 3(d), 4(a), 4(b), 4(d), 4(e), 5(b), and 5(f)]. Differences are observed near the front, where some drops and bubbles appear in Basilisk as numerical artifacts at  $\theta = 16^\circ$ . These artifacts are due to Basilisk's flow description. Indeed, as grains and air are both described as incompressible materials, the process of bubble formation and dynamics is not physically appropriate in the model. These instabilities get stronger as the slope angle increases due to increased flow front velocity.

However, the stopping “waves” initiation behavior is in qualitatively good agreement between the three models. Indeed, for all of them, the stopping waves start at times close to the stopping of the front at  $\theta = 0^\circ$  [Figs. 4(a)–4(c)] while they start at the left wall before the front stopping at  $\theta = 16^\circ$  [Figs. 4(d)–4(f)], even though this is less clear for the Navier-Stokes model.

**3. Stopping phase**

The spatiotemporal characteristics of the stopping phase are different in the three models. The thin-layer model stopping phase is the fastest since at  $\theta = 0^\circ$  the whole mass stops shortly after the front and at  $\theta = 16^\circ$  the front is the last part of the mass to stop [(Figs. 4(c) and 4(f)]. Indeed, a flow column will stop as soon as driving forces related to inertia, gravity, and surface slope drop below  $gh \cos(\theta)\mu(I)$ . Thus, contrary to Basilisk and COCD models, vertically distributed

movement (where the base of the flow is at rest but its top is still moving) is not modeled. However, even if the surface flows are expected to slightly remodel the deposit shape, the deposits obtained by SHALTOP are in excellent agreement with experiments, especially for the inclined plane, see Fig. 3(f). Indeed, as the slope angle increases, the flow gets thinner and therefore is better suited to be described by the thin-layer approximation.

The longest stopping phase is with the COCD, see Figs. 4(a) and 4(d). At  $\theta = 0^\circ$ , the stopping wave, initiated at the front and propagating backwards [see Figs. 4(a), 5(g), and 5(h)] is in good qualitative agreement with the 3D granular collapse experiments of similar aspect ratio (see Sec. 4.2 of Ref. [56]). The most significant difference with the experiment is observed for the discrete model at  $\theta = 16^\circ$ , where the flow is still moving after 1 s [Fig. 3(f)] and stops after  $t = 6.3$  s [Fig. 4(g)]. This large delay before the mass stopping at  $\theta = 16^\circ$  is due to the 2D configuration (see Sec. V E).

Finally, the time delay between the initiation of the stopping and the full stopping of the mass in the Navier-Stokes model is in between the time delay obtained with the other models at  $\theta = 0^\circ$  [Fig. 4(b)] and similar to the thin-layer model at  $\theta = 16^\circ$ . The Navier-Stokes model provides the closest deposits to the experiments, see Fig. 3. Interestingly, for  $\theta = 0^\circ$ , it is the unique model that generates three stopping waves, see Fig. 4(b). However, a thin layer (lower than 3.5 mm) is still in motion at a low velocity (between 1 and 3 cm s<sup>-1</sup>) for  $t \geq 1.2$  s, see Fig. 4(e). The Basilisk code solves the  $\mu(I)$ -rheology model, which incorporates a yield stress, allowing, in principle, for an accurate description of solid regions. However, it faces the technical challenge of the flow front not completely stopping. Indeed, the regularization method used by Basilisk (see, e.g., Ref. [30]) approximates the yield stress by assigning a high but finite viscosity, resulting in incomplete stopping. Despite this approximation remaining well-suited for short-duration phenomena considered in this article, overcoming this issue could be achieved by increasing the maximum viscosity (or adjusting the regularization parameter) (Fig. 9 of Ref. [33]). However, this may lead to increased computational costs. Note that the augmented Lagrangian method is able to overcome the stopping issue at a lower computational cost than the regularization method with a high maximum viscosity (see, e.g., Refs. [31,32]). However, in our case of short-duration flows, the augmented Lagrangian method would lead to unnecessary increased computational costs.

Moreover, let's consider  $U$ , the typical horizontal velocity scale of a granular flow on an inclined plane with an angle  $\theta$ . This velocity is given by  $U = \sqrt{gH \cos \theta}$  [1], where  $g$  is the gravitational constant and  $H$  is the initial height of the mass. Hence, we obtain a characteristic horizontal velocity for each of the aspect ratios  $a = 0.31, 0.7, \text{ and } 1.24$ , where the slowest one is  $U = 0.94 \text{ m s}^{-1}$ . Thus, the velocity threshold of  $0.01 \text{ m s}^{-1}$  chosen to characterize the static (fluid) transition is nearly 100 times smaller than the smallest typical horizontal velocity. Consequently, the velocities of the nonzero fronts observed in Fig. 4 are well below the characteristic horizontal velocity scales of the considered flows.

The stopping phase appears to have excellent characteristics to discriminate the models and, in particular, the

appropriate rheological laws. Thus, qualitative and quantitative comparison with the stopping phase observed in laboratory experiments would be very interesting (e.g., Sec. 4.4 and Fig. 4 of Ref. [56]), but we do not have such data for these experiments. Indeed, contrary to flow profiles, accessing measurements inside the moving granular mass to study the stopping phase is technically challenging in experiments.

When we compare our 2D simulations to the 2D profiles of the 3D experiments, we see that their deviation increases with the slope angle. This result is not surprising because, as the mass velocity increases, the conditions of our 2D simulations deviate from the experiments (for example, the boundary conditions are not well simulated). It is particularly clear for the discrete model because of its smaller avalanche angle in 2D than in 3D (see discussion in Sec. VE). Even for the Navier-Stokes model, which is closest to the experiments, the no-slip condition at the bottom becomes less valid as the slope angle increases ([4,31]). Finally, Basilisk's solver considers a nonmiscible multiphase flow, which can lead to drops and bubbles appearing at the front when the flow velocity is high.

### B. Differences in basal stresses

A significant part of the basal stress results from the weight of the granular column (i.e., hydrostatic pressure) for all three models; see Figs. 6(b) and 6(c) for  $x \geq 0.2$  m. Consequently, the difference between the absolute positions of the curves, related to the different models, is mainly due to the different local mass thicknesses. It explains why the basal normal stresses obtained with the three models are in good quantitative agreement if the free surfaces are similar at a given position.

As the increase of bed inclination favors mass spreading, flow thickness is reduced. Thus, the weight of the grains is smaller at  $\theta = 16^\circ$  than at  $\theta = 0^\circ$ . It is why the basal stresses simulated with the continuum models (thin-layer and Navier-Stokes) at  $\theta = 16^\circ$  are much smaller than at  $\theta = 0^\circ$  despite higher velocities [compare Fig. 7(a) with 7(d), 7(b) with 7(e), and 7(c) with 7(d)]. The perturbation that appears in the basal stress  $\sigma_b$  with the thin-layer model at  $\theta = 16^\circ$  can be directly associated with the formal expression of  $p_b$  in SHALTOP [see Eq. (B7)]. The spatial derivatives of the velocity result in numerical artifacts since the velocity is not twice differentiable at the static (flowing) transition.

In the Navier-Stokes simulation, the basal normal stress  $\sigma_b$  may be different from the hydrostatic pressure  $p_h$  [Fig. 6(a)], but is relatively similar to the pressure  $P$ , indicating that deviatoric stresses are small (Fig. 7). When  $\sigma_b \geq p_h$ , a significant vertical motion induces a higher basal stress than the hydrostatic pressure. However, it is not clear how the stress  $\sigma_b$  can be lower than  $p_h$ . However, it is similar to what is observed in simulations obtained with the discrete model.

The most crucial difference for basal normal stresses is between the continuum and discrete models. Indeed, the discrete basal stress depends on the dynamics of colliding beads and on the geometry of the granular lattice varying with both space and time; see Ref. [87]. The discrete stress  $\sigma_b$  highly fluctuates around the hydrostatic pressure  $p_h$  (Figs. 6 and 7). During the flow, multiple grain rearrangements change force

chain distribution within the granular media, leading to strong variations in the basal stress: As a result, a small surface at the bottom of the flow may well carry more, or less, than the weight of the granular column of grains above it. These stress fluctuations increase with the slope (compare the two rows in Fig. 7). It is consistent with experiments and models discussed in Ref. [44], showing that the ratio between force fluctuations and the mean force at the base of granular flows increases with increasing inertial number  $I$ . These fluctuations decrease during the stopping phase (Fig. 6). Indeed, as successive collisions progressively dissipate energy with time,  $\sigma_b$  depends more and more on the static distribution of weight through the granular lattice and associated force chains rather than on dynamics contributions.

Another specific point in discrete model simulations is the decrease of  $\sigma_b$  close to the left wall (see Fig. 6). It is similar to the Janssen effect in a grain silo, where the stress is far from the hydrostatic pressure at the silo's bottom. Indeed, part of the granular weight is supported by the lateral walls [88,89]. In this simulation, the domain left wall contributes to the handling part of the granular weight that is not applied on the bottom. This particular stress profile can also be explained by the construction history of the granular column that strongly affects static stress distributions, as shown by Ref. [87] for a granular pile.

### C. Spectral analysis of discrete basal normal stress

Section IV C 2 shows that  $\sigma_b$  calculated from discrete simulations (COCD) display high frequency temporal variations, unlike continuum simulations where the basal stress varies at a slower pace. Consequently, the discrete model can be employed to examine high-frequency components arising from grain-to-grain interactions [3,85]. In contrast, the Navier-Stokes and thin-layer models primarily capture the low-frequency content associated with mass displacement [47,49]. To gain a comprehensive understanding of these distinctive characteristics in comparison to the other models, we investigate the dominant process responsible for generating these high frequencies in discrete simulations.

We analyze the spectral content of the basal stress as displayed in Figs. 8(a)–8(c), showing its spectrogram at the different probes  $x_i$ ,  $i = 1, 2, 3$  for  $\theta = 0^\circ$ . More precisely, we only consider here the fluctuations in the signals by subtracting the smooth signal (the dark-blue line) from the total signal (light-blue line) in Fig. 7. Figures 8(d)–8(f) are the spectrograms of these signals. The maximum frequency that can be measured here is 500 Hz, related to the time step of the discrete simulation ( $\Delta t = 0.001$  s). Acoustic measurements of waves generated by steady granular flows or dam breaks show that wave frequencies go up to tens of kHz in our conditions; see Refs. [42–45]. These frequencies are related to the Hertz contact, not accounted for in our CD framework simulations.

The main frequency observed is around 100 Hz for the three probes [Figs. 8(a)–9(c)], and the maximum frequency decreases as the distance of the probe increases and with time [Figs. 8(d)–8(f)]. The range of dominant frequencies [with an associated power higher than 150 in Fig. 8(a)] is 35–300 Hz. The corresponding periods (0.003–0.28 s) may correspond to

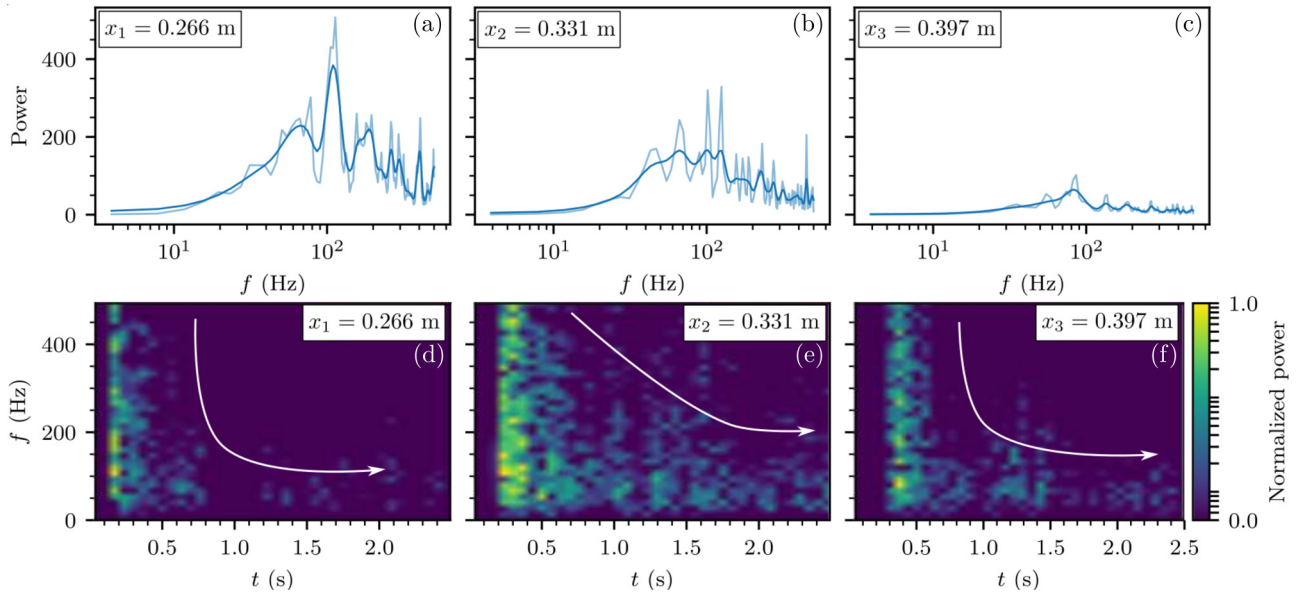


FIG. 8. Spectral content of the discrete (COCD) basal normal stress  $\sigma_b$  at  $\theta = 0^\circ$  computed at  $x_1 = 0.27$  m (a), (d);  $x_2 = 0.33$  m (b), (e); and  $x_3 = 0.40$  m (c), (f). The first line (a)–(c) is the spectral amplitude (light blue line: raw Fourier transform; dark blue line: smoothed Fourier transform). The second line (d)–(f) displays the corresponding spectrograms. The associated signals are given in Fig. 7.

the characteristic times  $t_{\text{macro}}$  for grain rearrangements due to the average shear between layers of grains, see Eq. (6.3) in Ref. [1], which would correspond to the so-called modulation frequency measured in granular flow experiments by Ref. [45] (their Figs. 9 and 10). For the three probes, Fig. 9 presents the mean frequency of layer frequencies  $f_{ij} = 1/t_{\text{macro},ij}$  related to the characteristic time  $t_{\text{macro},ij}$  related to the shear of layers in the mass thickness. More precisely,  $t_{\text{macro},ij} = d/|\Delta u_{ij}|$ ,  $i < j$  where  $d$  is the mean grain diameter and  $\Delta u_{ij}$  is the relative velocity between two connected layers (see details of its computation in Appendix B 3). Figure 9 shows that this mean frequency belongs to the range of dominant frequencies mentioned before. It enforces the hypothesis that the main event during the flow is related to the time  $t_{\text{macro}}$ , corresponding here to the average time for one bead from layer  $j$  to pass over one another bead from layer  $i$ . Further studies are needed to explore this hypothesis.

The total energy of the source decreases from the first to the third probe, probably because energy is progressively dissi-

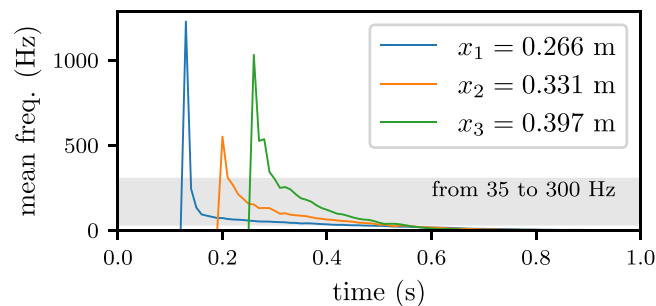


FIG. 9. For the three probes, the mean frequency of frequencies  $f_{ij}$  related to characteristic times  $f_{ij} = 1/t_{\text{macro},ij}$  related to the shear of layers  $i, j$  in the mass thickness (see details of this computation in Appendix B 3).

pated within the granular media. Lab experiments of granular collapses and generated acoustic waves showed that the radiated energy decreases before the deceleration phase of the front (see Figs. 8(a) and 8(b) of Ref. [42]). The deceleration phase at  $\theta = 0^\circ$  is starting around 0.2 s here, so when the front arrives at probes  $x_2$  and  $x_3$  it has already decelerated.

The spectrograms [Figs. 8(d)–8(f)] highlight that most energy is radiated when the flow front reaches the probes, at times  $t = 0.1, 0.2,$  and  $0.3$  s for  $x_1, x_2,$  and  $x_3$ . One can distinguish two behaviors: for  $x_1$  and  $x_3$  [Figs. 8(d) and 8(f)], most of the energy is radiated in the first 0.3 to 0.4 s after the front arrives. The associated frequency bandwidth is 30–400 Hz, with main frequencies between 100 and 200 Hz. Afterward, generated frequencies hardly exceed 175 or 200 Hz. On the contrary for  $x_2$ , in the first 0.3 s following the front arrival, energy is almost evenly distributed over the 30–300 Hz frequency bandwidth [Fig. 8(e)]. Besides, contrary to the other probes, the decrease in energy radiation and frequency bandwidth is more progressive and lasts more than 1 s [compare white arrows in Figs. 8(d)–8(f)].

The behavior at  $x_2$  compared to  $x_1$ , and  $x_3$  may be explained by the fact that the flow is more transient at  $x_1$  (quick acceleration near the initial mass) and  $x_3$  (flow stop quickly after arrival) than at  $x_2$  where the flow decelerates progressively. Furthermore, at  $x_1$ , after the front passes, the grains near the base are almost static and the moving grains near the free surface are far from the base [see Figs. 5(e)–5(h)], so the stress fluctuations from the upper grains hardly reach the base. For  $x_3$ , at  $t = 0.5$  s there is almost no moving grains above the front, so the stress fluctuation decreases rapidly [see Fig. 4(a)]. Then  $x_2$  has an intermediate behavior. Indeed, at this position, the grains near the free surface are still moving until about 0.8 s [Fig. 5(h)] and, as the flow thickness is quite small at this position [around 2.5 cm corresponding to  $\sim 3$  beads, Fig. 3(b)], the associated stress fluctuations may propagate down to the base during the relaxation phase of the upper

grains up to full stopping of the mass. However, given the strong spatial variation of the basal normal stress and the role of force chains in the stress transmission, a deeper analysis of these processes should be performed, which is beyond the scope of this article.

The spectrograms in Fig. 8 can be qualitatively compared to those obtained in laboratory experiments, from the bottom force measured at the arrival of an avalanche at a given location (see Fig. 3(a) of Ref. [44]). In these measurements, the front arrival signature is similar to that calculated here, even if their dominant frequencies are much higher. The spectrogram at probe  $x_2$  in our study [Fig. 8(e)] is closer to the experimental spectrogram which has been measured for a granular mass reaching a steady-uniform regime some time after the front arrival.

Note that a pulse of energy can be observed at all probes at about 1.1–1.4 s, more visible at  $x_3$  [Fig. 8(f)]. This regain of radiated energy is related to the full stopping of the mass as can be seen in Fig. 4(a).

#### D. Influence of rheological parameters

##### 1. Rheological parameters in continuum simulations

To compare the different models considered in this article, we chose a set of parameters that proved to reproduce rather correctly the evolution of the flow free surface in the case  $\theta = 0^\circ$ . However, the determination of appropriate rheology for granular flow modeling and the choice of corresponding rheological parameters are still open issues.

Considering the  $\mu(I)$  rheology for the dam-break simulations, several values of  $\mu_1$ ,  $\mu_2$ , and  $I_0$  can be found in the literature, all being specifically defined either in experimental or numerical studies. For instance, Jop *et al.* [74] experimentally measured

$$\mathcal{R}_{\text{Jop}} = \{\mu_1 = 0.382, \quad \mu_2 = 0.644, \quad I_0 = 0.279\}, \quad (17)$$

whereas Ref. [21] obtained, by calibrating  $\mu(I)$  with axisymmetric DEM simulations, that the best fit to their data was

$$\mathcal{R}_{\text{Lac}} = \{\mu_1 = 0.40, \quad \mu_2 = 0.70, \quad I_0 = 0.3\}, \quad (18)$$

and Ref. [30] chose

$$\mathcal{R}_{\text{Lag}} = \{\mu_1 = 0.32, \quad \mu_2 = 0.60, \quad I_0 = 0.4\} \quad (19)$$

to match the results obtain with the Navier-Stokes Gerri's flow solver to 2D-DEM simulations. Based on a previous study comparing numerical simulations to experimental dam breaks, Ref. [31] defined the friction parameters in their continuous models as

$$\mathcal{R}_{\text{Ion}} = \{\mu_1 = 0.480, \quad \Delta\mu = 0.250, \quad I_0 = 0.279\}. \quad (20)$$

These last coefficients have explicitly been defined to match the experimental data of Ref. [16] by increasing the static friction coefficient  $\mu_1$  to consider the effect of the lateral walls on the spreading of the granular column. Indeed, at the moment, the frictional dissipation due to lateral walls cannot be taken into account otherwise in 2D simulations. It should be noted that Ref. [32] added two times wall effects (in the friction coefficient and in the additional force related to wall effects) to reproduce laboratory-scale experiments at high slopes ( $\theta = 22^\circ$ ).

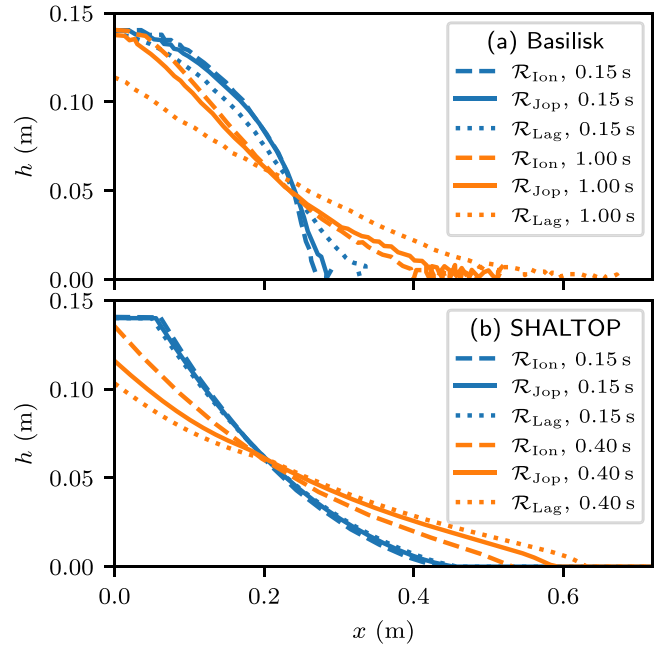


FIG. 10. Influence of  $\mu(I)$ -rheology parameters on simulation results for  $a = 0.7$  and  $\theta = 0^\circ$ . We display flow profiles at  $t = 0.4$  s and  $t = 1.0$  s. (a) Basilisk simulations with parameters from Ref. [31] (used in previous figures,  $\mathcal{R}_{\text{Ion}}$ ), parameters from Ref. [74] ( $\mathcal{R}_{\text{Jop}}$ ), and from Ref. [30] ( $\mathcal{R}_{\text{Lag}}$ ). (a) SHALTOP simulations with parameters  $\mathcal{R}_{\text{Ion}}$ ,  $\mathcal{R}_{\text{Jop}}$ , and  $\mathcal{R}_{\text{Lag}}$ .

To better evaluate the effect of the frictional coefficients in the  $\mu(I)$  rheology, a comparison between  $\mathcal{R}_{\text{Ion}}$ ,  $\mathcal{R}_{\text{Jop}}$ , and  $\mathcal{R}_{\text{Lag}}$  is presented in Fig. 10. As expected, the lower the friction coefficients, the longer the run-out distance. The longest is obtained using  $\mathcal{R}_{\text{Lag}}$ , then  $\mathcal{R}_{\text{Jop}}$ , and, finally,  $\mathcal{R}_{\text{Ion}}$ . However, note that the initial dynamics are relatively similar, at least during the first 0.15 s. It suggests that the differences between the thin-layer and Navier-Stokes dynamics may be still qualitatively similar to those analyzed in this article for a wide range of parameters.

##### 2. Friction coefficient in discrete COCD simulations

In discrete simulations, it is also nontrivial to choose the friction coefficient. In Ref. [90], a table with values used in the literature is given: they range between  $\mu_p = 0$  and  $\mu_p = 1$ . The influence of the friction coefficient in COCD simulations can be found in Fig. 5 of Ref. [52]: it obviously shows that the smaller the coefficient of friction, the greater the distance reached by the front. However, the difference is small (about 15% between  $\mu = 0.2$  and 0.8), especially compared to the influence of the 2D versus 3D discrete simulations (see Sec. VE).

#### E. Influence of simulation geometry

In this article, we have considered that the granular flow dynamics does not change in the direction transverse to the flow. As discussed in the previous section, it is not true in reality, as lateral walls can have a significant impact on the flow [31]. This effect is oversimplified here and tackled by empir-

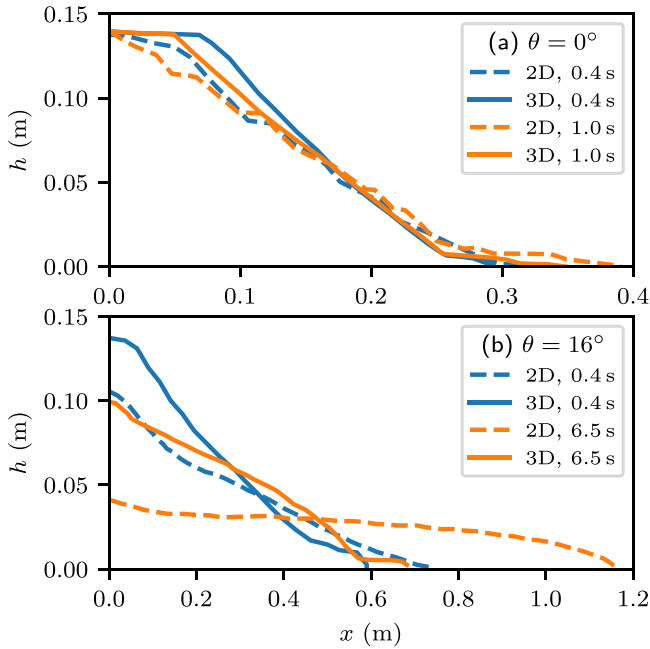


FIG. 11. Influence of the space dimension on the discrete model COCD results for  $\theta = 0^\circ$  (a) and  $\theta = 16^\circ$  (b). The aspect ratio is  $a = 0.7$ . The friction coefficient is exactly the same between the 2D and 3D simulations,  $\mu_p = 0.9$ . We display flow profiles at  $t = 0.4, 1.0,$  and  $6.5$  s. At  $\theta = 16^\circ$  (b), the 3D simulation is at rest at  $1.63$  s.

ically increasing friction coefficients of the  $\mu(I)$  rheology in continuum models (e.g., Ref. [32] for wall effects, although they are considered two times as discussed previously).

As explained in Appendix A, SHALTOP’s implementation does not solve the thin-layer equations in a 2D domain, and we have to solve them in a 3D domain; that is, we solve for the depth-averaged velocity field  $\bar{V}_x(x, y, t)$  in a channel of arbitrary width  $W$  and use lateral boundary conditions and initial conditions to ensure that  $\bar{V}_x$  does not depend on  $y$ . With this method, SHALTOP proved to reproduce the 2D thin-layer dam-break problem’s analytical solution accurately. Thus, we can be confident that our simulation results do not depend on the width  $W$  of the channel used in simulations and are consistent with the 2D thin-layer equations.

In COCD simulations, the 2D equations describe the motion of discs, whereas the 3D equations describe the motion of spheres. Figure 11 shows that with the same friction coefficient  $\mu_p$ , the repose angle is smaller in 2D than in 3D. For example, in Ref. [52], the maximal avalanche angle for 2D flows is about  $17^\circ$  when considering  $H_0/d = 15$ , with  $d$  the mean diameter of grains while it is above  $22^\circ$  in 3D, as in experiments [16,17]. The smaller value of the repose angle in 2D, compared to 3D, can be explained by the fact that in 3D, spheres can spread laterally, in the collapse transverse direction. It increases the number of potential traps but also the number of potential contacts, inducing a higher dissipation due to Coulomb friction between the grains. It explains, at least partly, why the friction coefficient we use in COCD simulations,  $\mu_p = 0.9$  (see Ref. [52]), must be higher than the friction coefficient between glass spheres estimated from experiments ( $0.2 \leq \mu \leq 0.3$ ), which is in the range between the

friction coefficient measured for a perfect glass-glass contact  $\mu = 0.4$  [70] and that empirically determined with MD models  $\mu = 0.16$ . Here, COCD runs in 2D because our goal is to compare the three models in the same 2D space configuration.

Here, we present the limit case for  $\theta = 16^\circ$  in 2D COCD simulations where the stopping is difficult but arises after a long duration [more than 6 s in Figs. 4(d) and 11(b)]. When considering a smaller inclination angle, the flow stops similarly to the two other models, see Fig. 12.

### VI. CONCLUSIONS

The comparison between discrete (COCD), Navier-Stokes (Basilisk), and thin-layer (SHALTOP) models for a simple granular dam-break simulation shows that they can reproduce the mass profiles measured in laboratory experiments with different levels of accuracy, provided an appropriate choice of the rheological parameters is made. The  $\mu(I)$  rheology is used here for both continuum models. The rheological parameters are kept constant for each model when simulating the granular collapses at three different angles from horizontal to  $\theta = 16^\circ$ . Even if the differences between the models strongly depend on the rheological parameters and simulation setups, general conclusions could be made:

(1) The thin-layer model overestimates the initial acceleration and velocity compared to other models and to the experiments, although the final deposits are consistent with the Navier-Stokes simulation with the same values of the  $\mu(I)$  rheology (except the volume fraction  $\Phi$  that has, however, only a limited influence on simulation results) and with the experiments. This result is important to validate the relevance of using thin-layer models for operational hazard assessment, and, in particular, to estimate the final mass distribution, travel distance, and dynamic impact of potential landslides. Indeed, as they require fewer computing resources than non-depth-integrated models, thin-layer models are often used by practitioners and experts.

(2) The Navier-Stokes and 2D discrete simulations have the same acceleration and deceleration phases but differ in the stopping phase. After the front stops, more and deeper particles are still in motion in the discrete simulations. The thin-layer simulations are globally faster than the two others in the three phases.

(3) 2D discrete simulations thus require an artificially higher interparticle friction coefficient when compared to 3D experiments (laterally confined flow here). In particular, in 2D discrete simulations using the same friction coefficient between the beads for slopes  $\theta = 0^\circ$  and  $\theta = 16^\circ$  results in a flow lasting several seconds too long at  $\theta = 16^\circ$ .

(4) For  $\theta = 16^\circ$ , the flow front is hardly managed in the Navier-Stokes code Basilisk with the apparition of artificial bubbles whose number increases as the slope angle increases.

(5) The basal normal stress measured from the Navier-Stokes and thin-layer models are qualitatively similar since they mainly depend on the flow thickness even though slightly higher variations are simulated with the Navier-Stokes model, which may be due to nonhydrostatic effects. The basal stress resulting from the discrete model is much more complex, with important spatial and temporal fluctuations at much higher frequencies, related to the grain-scale motion.

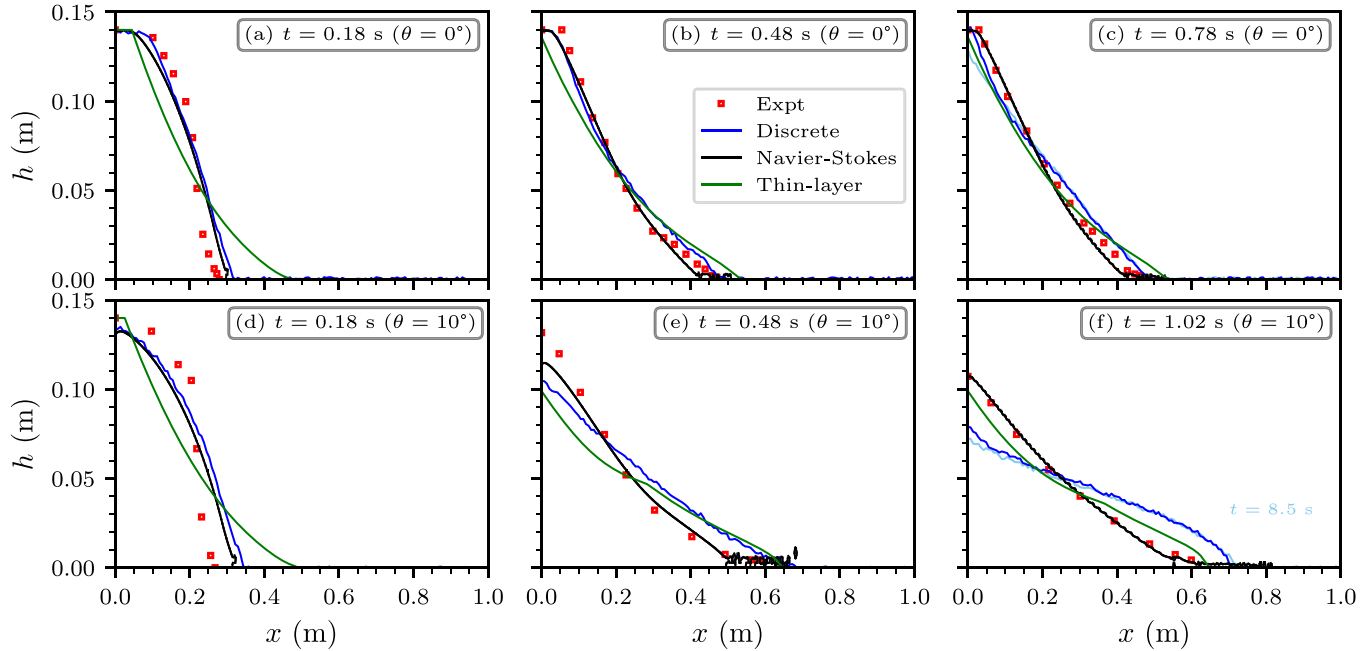


FIG. 12. Comparison between experiments and numerical simulations of the granular profiles during a dam break. We display the experimental results (red squares), discrete COCD simulations (blue line), Navier-Stokes Basilisk simulations (black line), and thin-layer SHALTOP simulations (green line). The initial aspect ratio is  $a = 0.7$ , with a bed slope  $\theta = 10^\circ$  (a)–(c), and  $\theta = 10^\circ$  (d)–(f). The light blue line in (c), (f) is the discrete simulation profile at  $t = 6.5$  s. At  $t = 1.02$  s in (f), the three codes are at rest.

A key point is that the differences between the models are more visible at higher slope angles. Furthermore, the characteristics of the basal stress and of the stopping phase appear to be much more discriminant for the models and rheology than the mass profiles during the collapse. This strongly suggests to use these quantities and consider the configuration of granular flows on sloping beds to assess the performance and limits of granular flow models and rheological laws or to calibrate the models. This is particularly important for modeling field-scale geophysical flows, when the simulated dynamics are compared to high and low frequency seismic recordings that give us a direct measurement of the basal stress applied by the landslide to the ground [47,49,91].

**ACKNOWLEDGMENTS**

This work was funded by Project No. ERC-CG-2013-PE10-617472 SLIDEQUAKES, DT-GEO European project (A Digital Twin for GEOphysical Extremes), and Institut Universitaire de France. Numerical computations were performed on the S-CAPAD plateforme, IPGP, France.

**APPENDIX A: NUMERICAL SETUP**

**1. Initial conditions**

The construction of the initial mass is straightforward in the Basilisk and SHALTOP simulations because it boils down to defining the boundary of the initial mass. In COCD (like in any DEM simulation), generating an initial state is more complex. The position, size, and number of beads must be defined. The way the initial column is built in COCD can strongly impact the initial force distribution in the granular media [87]. Following Ref. [87], the initial arrangement of

beads is constructed by simulating a uniform rain of beads (whose diameter follows a Gaussian distribution of mean  $d = 0.7$  mm and standard deviation 0.07 mm). It allows obtaining a granular network with a quasihydrostatic pressure [87]. However, in our initial box, the basal stress is not equal to the hydrostatic pressure, in particular, close to the left wall, as shown in Sec. IV C. A snapshot of the initial state is depicted in Appendix E (Fig. 13).

In experiments, we remark that the gate opening affects only the early stage of the collapse, as shown in Ref. [31]. Thus, in our simulations, we consider an instantaneous release of the initial granular mass (without accounting for the gate).

**2. Boundary conditions**

In COCD and Basilisk simulations, the beads and granular flow dynamics are solved directly in the 2D domain  $(x, z)$ , and no lateral boundary conditions are needed. On the contrary, SHALTOP solves the depth-averaged mass and momentum equations for flows on general 2D topographies  $Z = Z(X, Y)$  in a fixed vertical Cartesian frame  $(X, Y, Z)$  and not on 1D topographies  $Z = Z(X)$ . To mimic a 1D-topography problem, the topography is represented by an inclined plane of width  $W = 3 \times dx$  in the  $Y$  direction, with  $dx$  the numerical cell size. The initial mass spans the width of the grid uniformly. Then, a nonpenetration condition is set on the lateral boundaries of the grid, i.e., on  $Y = 0, Y = W$ .

A nonpenetration condition is also used on  $x = 0$  (or, equivalently, at  $X = 0$  for SHALTOP) in all three codes. This condition is done explicitly in COCD’s simulations through a vertical wall. This wall interacts with the particles with the same friction coefficient than for grain to grain contacts.



In Basilisk and SHALTOP, we impose  $V_x = 0$  and  $\bar{V}_X = 0$ , respectively.

The bottom boundary condition on  $z = 0$  is specific to each code. In COCD's simulations, as in experiments, a glued layer of beads is added to the bed. The size distribution of these glued beads is identical to the other grains. There is no space between two consecutive glued beads. Even if this is not really true because the glued beads could not move (e.g., role), this can be seen as a no-slip and nonpenetration condition, which is set explicitly in Basilisk [ $V_x(z = 0) = 0$  and  $V_z(z = 0) = 0$ ]. Note that in Navier-Stokes simulation of the same setup, Ref. [31] used a Coulomb friction condition at the base and studied the impact of this condition compared to the no-slip condition used here (see their Fig. 16 where deposit calculated with friction went about 0.04 m further than with no slip). In this article, a nonzero basal velocity was found near the front of the flowing mass (see their Fig. 18). As SHALTOP solves directly for the depth-average velocity  $\bar{V}_X$ , the bottom boundary condition is included in the equations and does not need to be specified numerically.

Note that thin-layer Eqs. (12) and (13) can be derived in two different manners. It is possible to use the no-slip condition and the internal  $\mu(I)$  rheology as in the Basilisk code. However, the same final equations are derived if we assume a Coulomb solid friction law at the interface between the flow and the topography, with a friction coefficient given by  $\mu(I)$  as in (11), and no condition on the bottom velocity (and thus on the velocity profile). See Chap. 1 in Ref. [92] for details.

## APPENDIX B: SIMULATION OUTPUT PROCESSING

To compare simulations, we extract key characteristics of the flow and we detail in this Appendix how they are calculated in each code.

### 1. Flow height and front position

For COCD's profiles, we first decompose the horizontal domain in cells of size  $d_x = 4d$ , where  $d = 0.7$  mm is the mean diameters of grains. The flow height is then defined, in each cell, as the height of the topmost beads. The front is computed with this same method without other postprocess.

One of Basilisk's outputs is directly the air (granular) media interface, represented in Fig. 3, from which the determination of the flow height  $h(x, t)$  is straightforward. Determining the flow front position is not straightforward because small drops detach from the main mass [e.g., Fig. 3(e)]. The  $\mu(I)$  rheology is no longer capable of modeling their propagation correctly, which may generate numerical issues. Indeed, due to these drops, the classical definition of the front position,

$$\hat{x}_f(t) = \max \{x, h(x, t) > 0\}, \quad (\text{B1})$$

does not yield an appropriate (i.e., physically relevant) position for the flow front. Instead, the front position  $x_f(t)$  is given by the intersection of the  $x$  axis with the tangent to the graph  $z_f(x) = h(x, t)$ , for  $x = \tilde{x}_f(t)$ .  $\tilde{x}_f(t)$  is the last position for which the flow height is positive for all abscissas before  $\tilde{x}_f(t)$ :

$$\tilde{x}_f(t) = \max \{X : \forall x < X, h(x, t) > 0\}. \quad (\text{B2})$$

In practice, before estimating the tangent, the graph  $z_f(x) = h(x, t)$  is smoothed (with a Lowess smoothing algorithm [93]). At time  $t_i$ ,  $x_f(t_i)$  is considered as an outlier if

$$\left| \frac{x_f(t_i) - x_m(t_i)}{x_m(t_i)} \right| > 0.01, \quad (\text{B3})$$

where

$$x_m(t_i) = 0.5(x_f(t_{i-1}) + x_f(t_{i+1})). \quad (\text{B4})$$

If Eq. (B3) is verified, then we set  $x_f(t_i) = x_m(t_i)$ . This rough filtering works because, in practice, we never had two outliers in a row.

In SHALTOP, the layer thickness  $h(x, t)$  is directly given as a simulation result. The flow front  $x_f(t)$  is then given by

$$x_f(t) = \min \{x, h(x, t) < 5d\}, \quad (\text{B5})$$

where  $d = 0.7$  mm is the mean diameter of beads in COCD-simulations.

### 2. Flow velocity and flow depth-integrated velocity

COCD computes every grain velocity. Let us consider the same domain decomposition described in Appendix B 1. At a given time  $t$ , we define the 2D columns of width  $dx$  and height  $h_{d_x}(x)$  for each cell and detect all the grains that belong to them. We then compute its horizontal mean velocity  $\bar{V}_x(x, t)$  for each column by averaging all the horizontal velocities of grains included in the column. The local horizontal velocity is the horizontal part of the velocity vectors of each grain.

Basilisk explicitly solves for the velocity field within the flow, that is,  $V_x(x, z, t)$  and  $V_z(x, z, t)$ . The depth-averaged flow velocity in the  $x$ -direction  $\bar{V}_x$  is then directly deduced following Eq. (13).

SHALTOP solves directly for the depth-averaged velocity  $\bar{V}$ , and no further processing is needed ( $V_x = \bar{V}$ ).

### 3. Basal stresses and pressures

For COCD, let us again consider the columns, introduced in precedent Appendix B 2. The probes have the same length  $dx$  as the columns. Since the grains belonging to each column can be detected, the total mass of the column is the sum of the masses of grains. In the computing of any grain mass  $m_i$ , we multiply the volume of disk  $i$  by the grain diameter  $d_i$  and by the glass density  $\rho = 2500$  kg m<sup>-3</sup>. We finally define the hydrostatic pressure  $p_h$  as being the column weight divided by the length (it would be the surface in 3D) of the bottom column  $d_x$ .

The basal normal stress  $\sigma_b$  is directly deduced from the resulting normal force applied on a probe (i.e., the resulting normal force applied on the four glued grains belonging to this probe) divided by its surface. It can be directly computed from the simulation results that include every contact force for all contacts at any time.

In SHALTOP, the hydrostatic pressure at the bottom of the flow is given by

$$p_h = \rho g \cos(\theta) h. \quad (\text{B6})$$

It is derived from the inviscid Navier-Stokes equations integrated into the topography normal direction (i.e., along the

$z$  axis), assuming that the stress tensor is  $\sigma = -pI_3$  and that  $V_z = 0$  at the bottom. Following Refs. [47,91] for more general cases where  $\sigma \neq -pI_3$ ,  $p_h$  is the leading term of the basal stress  $\sigma_b$  in the direction perpendicular to the topography. To get an accurate value of the basal stress, other terms from the asymptotic expansion must be included (see Eq. (3) in Ref. [47] and Eq. (5) in Ref. [91]). In the case of a flow over an inclined plane, an accurate value is

$$\sigma_b = p_h - \frac{\rho}{2} \left( \frac{\partial}{\partial t} \left( h^2 \frac{\partial V_x}{\partial x} \right) + \frac{\partial}{\partial x} \left( h^2 V_x \frac{\partial V_x}{\partial x} \right) \right). \quad (\text{B7})$$

In Basilisk, the basal stress  $\sigma_b$  is given by

$$\sigma_b = (\boldsymbol{\sigma} \mathbf{n}) \cdot \mathbf{n} \quad (\text{B8})$$

$$= \left( \begin{bmatrix} \eta_{\text{eff}} \dot{\gamma}_{xx} - P & \eta_{\text{eff}} \dot{\gamma}_{xy} \\ \eta_{\text{eff}} \dot{\gamma}_{xy} & \eta_{\text{eff}} \dot{\gamma}_{yy} - p \end{bmatrix} \begin{bmatrix} 0 \\ -1 \end{bmatrix} \right) \cdot \begin{bmatrix} 0 \\ -1 \end{bmatrix}, \quad (\text{B9})$$

$$\sigma_b = \eta_{\text{eff}} \frac{\partial v}{\partial y} - P \quad (\text{B10})$$

with

$$\eta_{\text{eff}} = \frac{\mu(I)P}{|\dot{\gamma}|} \quad (\text{B11})$$

and  $P$  the pressure, defined as the mean total stress.

Regarding the mean frequency presented in Fig. 9, it is computed as the average of multiple frequencies  $f_{ij}$ . We decompose the mass height in layers of width  $3d$ , with  $d$ , the mean diameter of grains. For each layer  $i$ , the mean along-slope velocity  $u_{x,i}$  is computed in a horizontal range of size  $20d$ , centered in each probe position. It is the velocity of grains belonging to layers of height  $3d$  and horizontal size  $20d$ , centered in  $x_i$ ,  $i = 1, 2, 3$ . We then compute the relative velocities between two successive layers  $\Delta u_{ij} = u_{x,j} - u_{x,i}$ ,  $j > i$  and the time  $t_{\text{macro},ij}$  is then computed as

$$t_{\text{macro},ij} = \frac{d}{|\Delta u_{ij}|}.$$

By definition,  $t_{\text{macro},ij}$  corresponds to the duration needed for a grain from the above layer  $j$  to go over a grain in the layer below  $i$ . The definition can be found in Ref. [1] [Eq. (6.3)]. Finally, the mean frequency presented in Fig. 9 is the average of frequencies  $f_{ij} = 1/t_{\text{macro},ij}$ .

## APPENDIX C: COMPUTATIONAL COSTS

We do not perform a detailed comparison of computational costs in this article, as our focus is on comparing these three physical models rather than their numerical solution methods and possible implementations. For each of the three models, various numerical solution methods exist, as well as multiple implementation algorithms (computer codes) for these methods. As this would constitute a separate study, we only indicate the orders of magnitude of the computation times required for conducting our simulations. It should be noted that the codes were executed on different machines, further adding to the complexity of their comparison.

Simulations of the discrete model were conducted using the COCD code on two Intel Xeon E5-2650 2.00 GHz  $2 \times 8$  cores) processors on the S-CAPAD platform, IPGP, France. On average, they required about 10 h of computation time for a 6.5 s flow simulation.

Simulations of the Navier-Stokes model were performed using the Basilisk code on an Intel Xeon(R) W-2125 4.00 GHz processor. On average, they required 7 h of computation time for a 2 s flow simulation. Note that a constant mesh on the entire domain has been used here.

Simulations of the thin-layer model were carried out using the SHALTOP code on a 12th Gen Intel(R) Core(TM) i5-12500H processor, 2.50 GHz, 32 GB RAM. On average, they required less than 1 min and 45 s of computation time for a 2 s flow simulation.

## APPENDIX D: NUMERICAL PARAMETERS

Table I in Appendix D provides all the numerical parameters that have been used to perform the simulations presented in this article using the three models.

TABLE I. Values of numerical parameters.

Description	Parameter	Value(s)
<i>Discrete, COCD</i>		
Beads mean diameter	$d$	0.7 mm
Beads diameter standard deviation	$s_d$	0.07 mm
Number of beads at $0^\circ$ , $10^\circ$ , and $16^\circ$	$N$	74 293
Friction coefficient	$\mu_p$	0.9
<i>Navier-Stokes, Basilisk</i>		
Size of grid cells in $x$ direction	$dx$	2.7 mm
Size of grid cells in $z$ direction	$dz$	2.7 mm
Parameters for the $\mu(I)$ rheology	$\mu_1, \mu_2, I_0$	(0.48, 0.73, 0.279)
<i>Thin-layer, SHALTOP</i>		
Size of grid cells in horizontal direction	$dX$	0.6 mm
Parameters for the $\mu(I)$ rheology	$\mu_1, \mu_2, I_0$	(0.48, 0.73, 0.279)

**APPENDIX E: EXTENDED DATA**

Figure 13 depicts the initial configuration of the granular mass. The zoom performed in the red rectangular area allows for a better understanding of the sizes of the different grids in relation to the system size. The discrete model involves spherical grains with an average diameter of 0.7 mm. The Navier-Stokes model considers a space composed of square cells with sides measuring 2.7 mm, and the thin-layer model employs cells with heights equal to the free surface height and with a constant width of 0.6 mm.

Figures 14 to 17 display the results of simulations conducted with different aspect ratios ( $a = 0.31$  and  $1.24$ ) than the one used throughout the rest of the article ( $a = 0.7$ ). Figures 14 and 15 provide snapshots of the flow, along with experimental data, while Figs. 16 and 17 present spatio-temporal plot of the depth-averaged along-slope flow velocity. These four figures demonstrate that the results presented in this article are not dependent on the aspect ratio of the initial mass configuration, whether it is small ( $a = 0.31$ , resulting in a spread-out mass) or large ( $a = 1.24$ , resulting in a vertical mass).

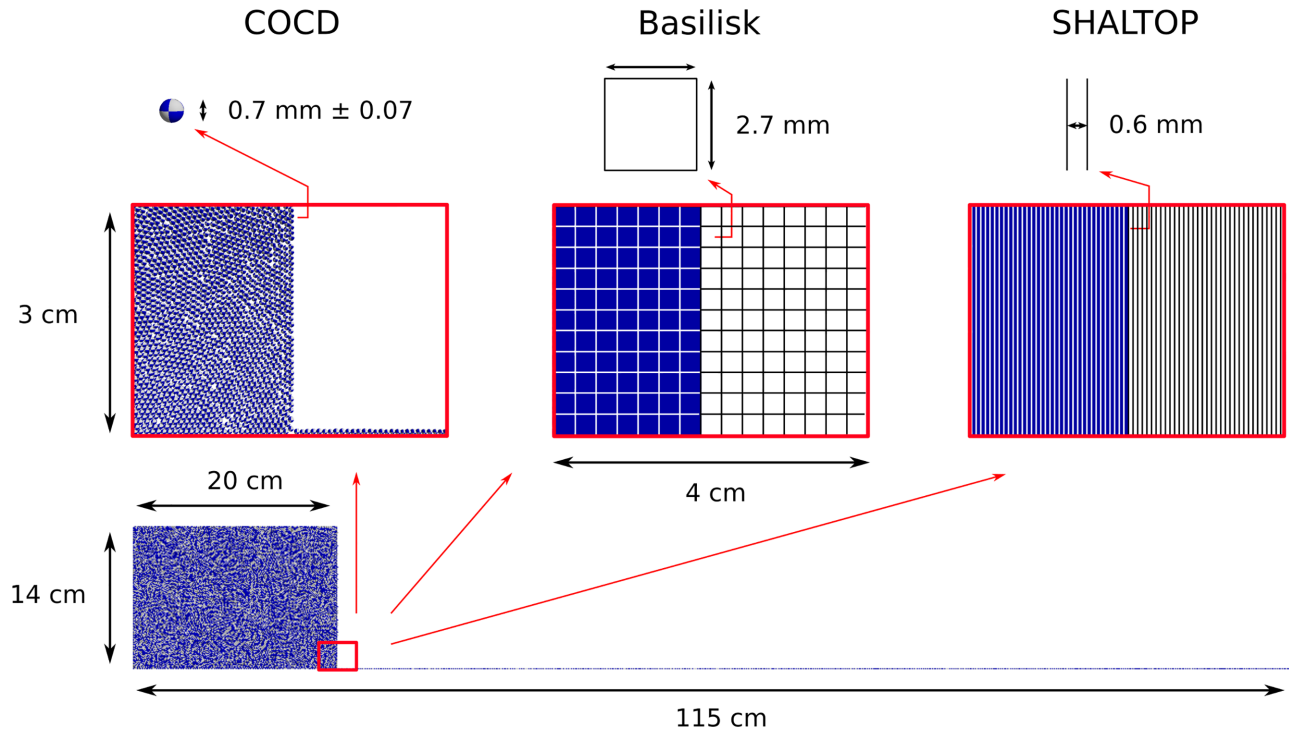


FIG. 13. Snapshot of the initial state for an aspect ratio of  $a = 0.7$ . The red boxes represent a rectangular area of size  $4 \times 3$  cm located near the front, allowing us to observe the fine grids used by Basilisk and Shaltop, as well as the size of grains simulated by COCD.

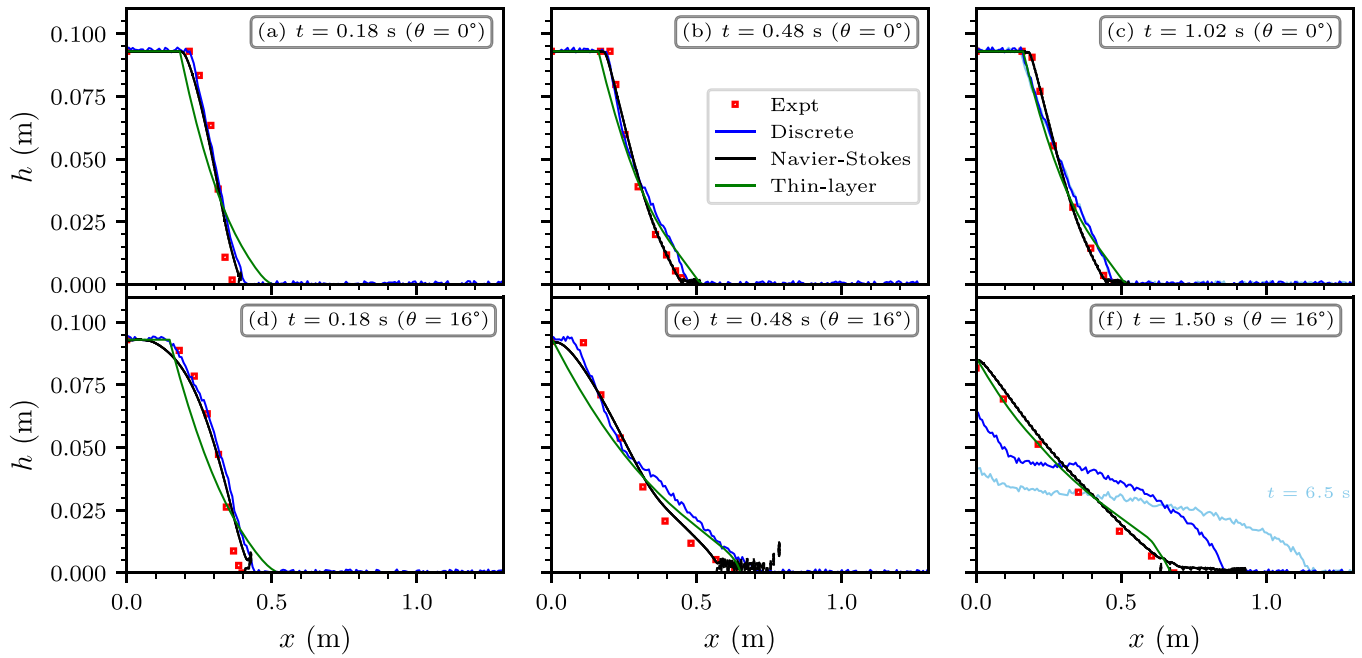


FIG. 14. Comparison between experiments and numerical simulations of the granular profiles during a dam break. We display the experimental results (red squares), discrete COCD simulations (blue line), Navier-Stokes Basilisk simulations (black line), and thin-layer SHALTOP simulations (green line). The initial aspect ratio is  $a = 0.31$ , with a bed slope  $\theta = 0^\circ$  (a)–(c) and  $\theta = 16^\circ$  (d)–(f). The light blue line in (c), (f) is the discrete simulation profile at  $t = 6.5$  s.

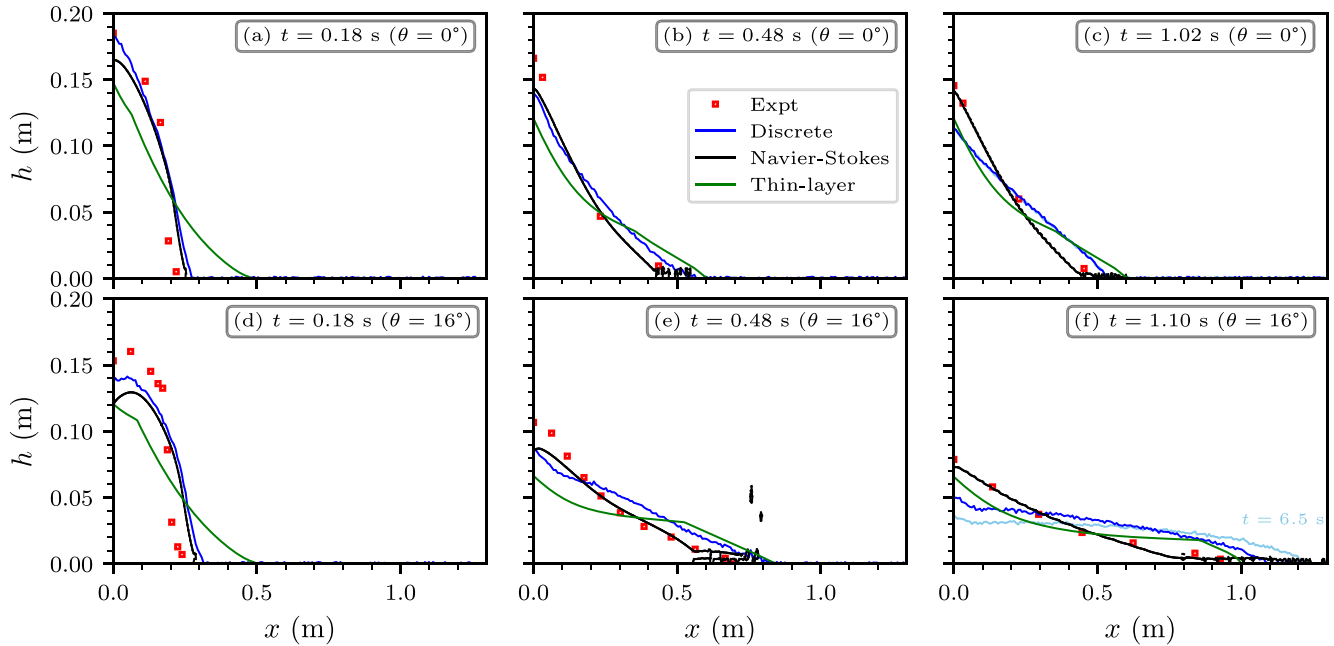


FIG. 15. Comparison between experiments and numerical simulations of the granular profiles during a dam break. We display the experimental results (red squares), discrete COCD simulations (blue line), Navier-Stokes Basilisk simulations (black line), and thin-layer SHALTOP simulations (green line). The initial aspect ratio is  $a = 1.24$ , with a bed slope  $\theta = 0^\circ$  (a)–(c) and  $\theta = 16^\circ$  (d)–(f). The light blue line in (c), (f) is the discrete simulation profile at  $t = 6.5$  s.

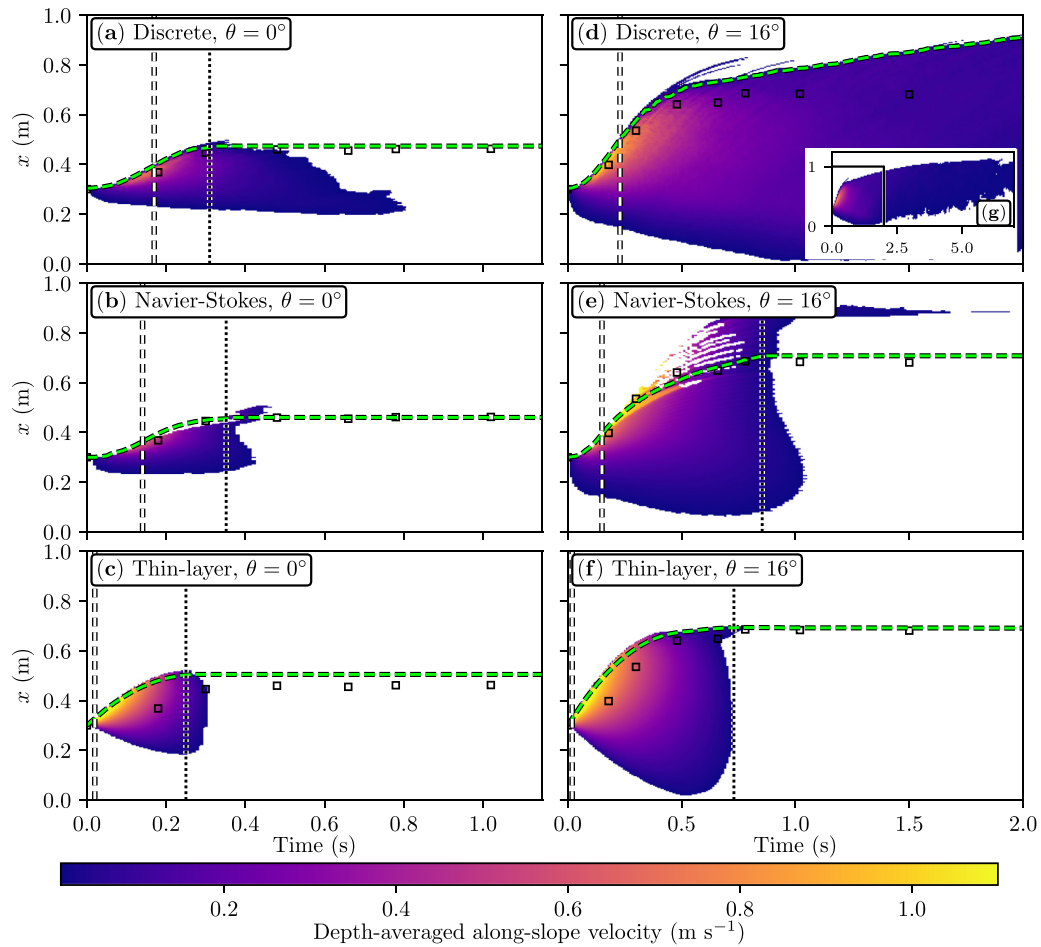


FIG. 16. Spatiotemporal plot representing the depth-averaged along-slope flow velocity  $\bar{V}_x(x, t)$  (color scale) for the different models, with  $\theta = 0^\circ$  (a)–(c) and  $\theta = 16^\circ$  (d)–(f). The initial aspect ratio is  $a = 0.31$ . We only display velocities above  $1 \text{ cm s}^{-1}$  (lower velocities are represented in white), as in the experiments of Ref. [17]. Black squares give the front position in experiments.

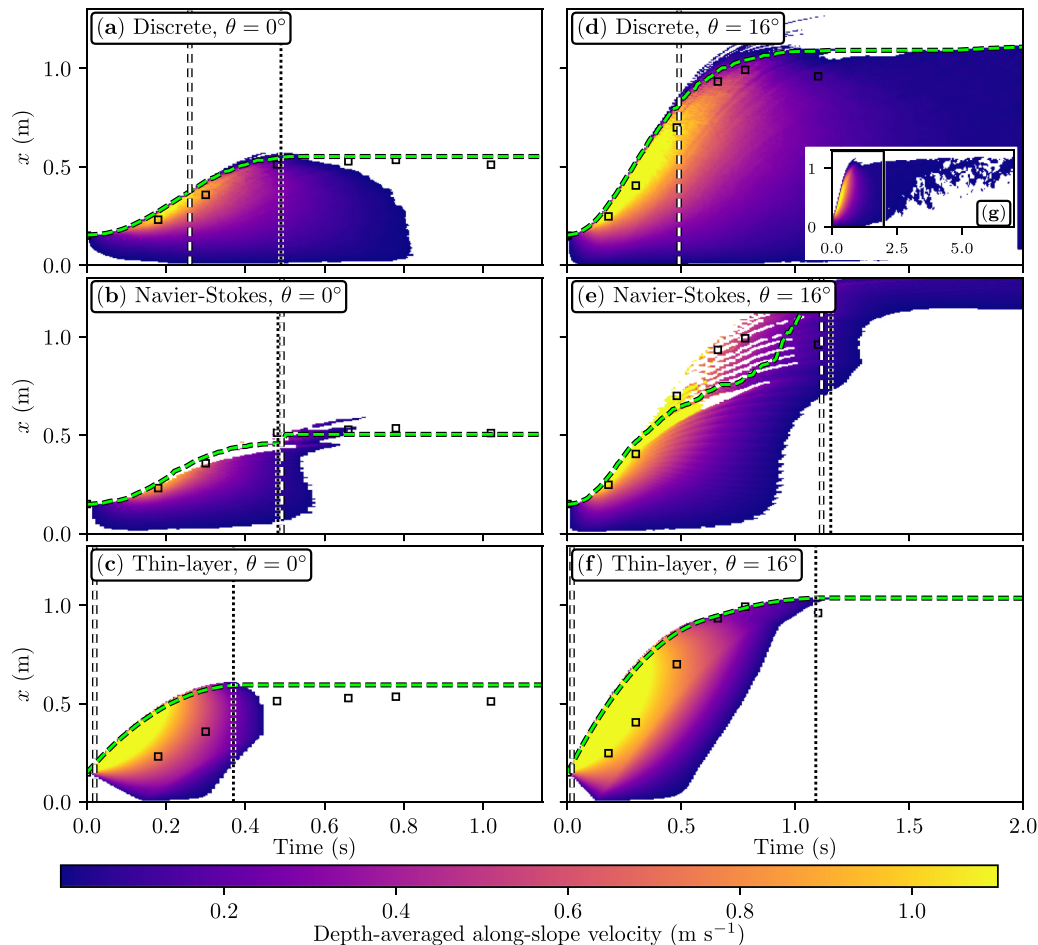


FIG. 17. Spatiotemporal plot representing the depth-averaged along-slope flow velocity  $\bar{V}_x(x, t)$  (color scale) for the different models, with  $\theta = 0^\circ$  [(a)–(c)] and  $\theta = 16^\circ$  [(d)–(f)]. The initial aspect ratio is  $a = 1.24$ . We only display velocities above  $1 \text{ cm s}^{-1}$  (lower velocities are represented in white), as in the experiments of Ref. [17]. Black squares give the front position in experiments.

- [1] B. Andreotti, Y. Forterre, and O. Pouliquen, *Granular Media: Between Fluid and Solid* (Cambridge University Press, Cambridge, UK, 2013).
- [2] J. L. Baker, C. G. Johnson, and J. M. N. T. Gray, Segregation-induced finger formation in granular free-surface flows, *J. Fluid Mech.* **809**, 168 (2016).
- [3] C. Hibert, A. Mangeney, G. Grandjean, and N. Shapiro, Slope instabilities in dolomieu crater, réunion island: From seismic signals to rockfall characteristics, *J. Geophys. Res.: Earth Surf.* **116**, F04032 (2011).
- [4] R. Delannay, A. Valance, A. Mangeney, O. Roche, and P. Richard, Granular and particle-laden flows: From laboratory experiments to field observations, *J. Phys. D* **50**, 053001 (2017).
- [5] D. Hantz, J. Corominas, G. B. Crosta, and M. Jaboyedoff, Definitions and concepts for quantitative rockfall hazard and risk analysis, *Geosciences* **11**, 158 (2021).
- [6] O. Hungr, Rock avalanche occurrence, process and modelling, in *Landslides from Massive Rock Slope Failure*, NATO Science Series, edited by S. G. Evans, G. S. Mugnozza, A. Strom, and R. L. Hermanns (Springer Netherlands, Dordrecht, 2006), pp. 243–266.
- [7] A. Strom and K. Abdrakhmatov, Quantitative relationships of Central Asian Bedrock Landslide parameters, in *Rockslides and Rock Avalanches of Central Asia* (Elsevier, Amsterdam, The Netherlands, 2018), pp. 335–347.
- [8] M. Peruzzetto, J. C. Komorowski, A. Le Friant, M. Rosas-Carbajal, A. Mangeney, and Y. Legendre, Modeling of partial dome collapse of La Soufrière of Guadeloupe volcano: Implications for hazard assessment and monitoring, *Sci. Rep.* **9**, 13105 (2019).
- [9] T. Esposti Ongaro, M. Cerminara, S. J. Charbonnier, G. Lube, and G. A. Valentine, A framework for validation and benchmarking of pyroclastic current models, *Bull. Volcanol.* **82**, 51 (2020).
- [10] V. Gueugneau, S. Charbonnier, T. Esposti Ongaro, M. Peruzzetto, A. Mangeney, F. Bouchut, A. Patra, K. Kelfoun *et al.*, Synthetic benchmarking of concentrated pyroclastic current models, *Bull. Volcanol.* **83**, 75 (2021).
- [11] O. Korup, D. Schneider, C. Huggel, and A. Dufresne, Long-runout landslides, in *Treatise on Geomorphology* (Elsevier, Amsterdam, The Netherlands, 2013), pp. 183–199.

- [12] A. Lucas, A. Mangeney, and J. P. Ampuero, Frictional velocity-weakening in landslides on Earth and on other planetary bodies, *Nat. Commun.* **5**, 3417 (2014).
- [13] G. Félix and N. Thomas, Relation between dry granular flow regimes and morphology of deposits: Formation of levées in pyroclastic deposits, *Earth Planet. Sci. Lett.* **221**, 197 (2004).
- [14] A. N. Edwards, S. Viroulet, B. P. Kokelaar, and J. M. N. T. Gray, Formation of levees, troughs and elevated channels by avalanches on erodible slopes, *J. Fluid Mech.* **823**, 278 (2017).
- [15] F. M. Rocha, C. G. Johnson, and J. M. N. T. Gray, Self-channelisation and levee formation in monodisperse granular flows, *J. Fluid Mech.* **876**, 591 (2019).
- [16] A. Mangeney, O. Roche, O. Hungr, N. Mangold, G. Faccanoni, and A. Lucas, Erosion and mobility in granular collapse over sloping beds, *J. Geophys. Res.: Earth Surf.* **115**, F03040 (2010).
- [17] M. Farin, A. Mangeney, and O. Roche, Fundamental changes of granular flow dynamics, deposition, and erosion processes at high slope angles: Insights from laboratory experiments, *J. Geophys. Res.: Earth Surf.* **119**, 504 (2014).
- [18] A. Edwards, S. Viroulet, C. Johnson, and J. Gray, Erosion-deposition dynamics and long distance propagation of granular avalanches, *J. Fluid Mech.* **915**, A9 (2021).
- [19] Y. Forterre and O. Pouliquen, Stability analysis of rapid granular chute flows: Formation of longitudinal vortices, *J. Fluid Mech.* **467**, 361 (2002).
- [20] A. Mangeney, F. Bouchut, N. Thomas, J.-P. Vilotte, and M.-O. Bristeau, Numerical modeling of self-channeling granular flows and of their levee-channel deposits, *J. Geophys. Res.: Earth Surf.* **112**, F02017 (2007).
- [21] L. Lacaze and R. R. Kerswell, Axisymmetric granular collapse: A transient 3D flow test of viscoplasticity, *Phys. Rev. Lett.* **102**, 108305 (2009).
- [22] P. A. Cundall and O. D. L. Strack, A discrete numerical model for granular assemblies, *Géotechnique* **29**, 47 (1979).
- [23] J. J. Moreau, Some numerical methods in multibody dynamics: Application to granular materials, *Eur. J. Mech. A. Solids* **13**, 93 (1994).
- [24] B. Maury, A time-stepping scheme for inelastic collisions, *Numer. Math.* **102**, 649 (2006).
- [25] F. Radjai, J.-N. Roux, and A. Daouadji, Modeling granular materials: Century-long research across scales, *J. Eng. Mech.* **143**, 04017002 (2017).
- [26] F. Radjai and F. Dubois, *Discrete-Element Modeling of Granular Materials* (Wiley-Iste, Hoboken, NJ, 2011).
- [27] L. Girolami, V. Hergault, G. Vinay, and A. Wachs, A three-dimensional discrete-grain model for the simulation of dam-break rectangular collapses: Comparison between numerical results and experiments, *Granular Matter* **14**, 381 (2012).
- [28] C. R. K. Windows-Yule, D. R. Tunuguntla, and D. J. Parker, Numerical modelling of granular flows: A reality check, *Comput. Part. Mech.* **3**, 311 (2016).
- [29] L. F. Orozco, J.-Y. Delenne, P. Sornay, and F. Radjai, Scaling behavior of particle breakage in granular flows inside rotating drums, *Phys. Rev. E* **101**, 052904 (2020).
- [30] P. Y. Lagrée, L. Staron, and S. Popinet, The granular column collapse as a continuum: Validity of a two-dimensional Navier-Stokes model with a  $\mu(I)$ -rheology, *J. Fluid Mech.* **686**, 378 (2011).
- [31] I. R. Ionescu, A. Mangeney, F. Bouchut, and O. Roche, Viscoplastic modeling of granular column collapse with pressure-dependent rheology, *J. Non-Newtonian Fluid Mech.* **219**, 1 (2015).
- [32] N. Martin, I. R. Ionescu, A. Mangeney, F. Bouchut, and M. Farin, Continuum viscoplastic simulation of a granular column collapse on large slopes:  $\mu(I)$  rheology and lateral wall effects, *Phys. Fluids* **29**, 013301 (2017).
- [33] C. Lusso, A. Ern, F. Bouchut, A. Mangeney, M. Farin, and O. Roche, Two-dimensional simulation by regularization of free surface viscoplastic flows with Drucker–Prager yield stress and application to granular collapse, *J. Comput. Phys.* **333**, 387 (2017).
- [34] M. Pirulli, A. Leonardi, and C. Scavia, Comparison of depth-averaged and full-3D model for the benchmarking exercise on landslide runout, in *Proceedings of the Second JTC1 Workshop on Triggering and Propagation of Rapid Flow-like Landslides* (The Hong Kong Geotechnical Society, Hong Kong, 2018).
- [35] A.-J.-C. Barré de Saint-Venant, Theory of unsteady water flows, with applications to river floods and tidal waves that can travel upstream their channels, *Comptes rendus hebdomadaires des séances de l'Académie des sciences* **LXXIII** (1871).
- [36] R. F. Dressler, New nonlinear shallow-flow equations with curvature, *J. Hydraul. Res.* **16**, 205 (1978).
- [37] S. B. Savage and K. Hutter, The dynamics of avalanches of granular materials from initiation to runout. Part I: Analysis, *Acta Mech.* **86**, 201 (1991).
- [38] S. McDougall, 2014 Canadian Geotechnical Colloquium: Landslide runout analysis—current practice and challenges, *Can. Geotech. J.* **54**, 605 (2017).
- [39] M. Pastor, K. Soga, S. McDougall, and J. S. H. Kwan, Review of benchmarking exercise on landslide runout analysis 2018, in *Proceedings of the Second JTC1 Workshop on Triggering and Propagation of Rapid Flow-like Landslides* (The Hong Kong Geotechnical Society, Hong Kong, 2018).
- [40] P. Poulain, A. Le Friant, R. Pedreros, A. Mangeney, A. G. Filippini, G. Grandjean, A. Lemoine, E. D. Fernández-Nieto, M. J. C. Díaz, and M. Peruzzetto, Numerical simulation of submarine landslides and generated tsunamis: Application to the on-going Mayotte seismo-volcanic crisis, *C. R. Géosci.* **354**, 361 (2022).
- [41] M. Peruzzetto, C. Levy, Y. Thiery, G. Grandjean, A. Mangeney, A.-M. Lejeune, A. Nachbaur, Y. Legendre, B. Vittecoq, J.-M. Saurel, V. Clouard, T. Dewez, F. R. Fontaine, M. Mergili, S. Lagarde, J.-C. Komorowski, A. Le Friant, and A. Lemarchand, Simplified simulation of rock avalanches and subsequent debris flows with a single thin-layer model: Application to the Prêcheur river (Martinique, Lesser Antilles), *Eng. Geol.* **296**, 106457 (2022).
- [42] M. Farin, A. Mangeney, J. De Rosny, R. Toussaint, and P.-T. Trinh, Link between the dynamics of granular flows and the generated seismic signal: Insights from laboratory experiments, *J. Geophys. Res.: Earth Surf.* **123**, 1407 (2018).
- [43] M. Farin, A. Mangeney, J. De Rosny, R. Toussaint, and P.-T. Trinh, Relations between the characteristics of granular column collapses and resultant high-frequency seismic signals, *J. Geophys. Res.: Earth Surf.* **124**, 2987 (2019).
- [44] M. I. Arran, A. Mangeney, J. De Rosny, M. Farin, R. Toussaint, and O. Roche, Laboratory landquakes: Insights from experiments into the high-frequency seismic signal generated by

- geophysical granular flows, *J. Geophys. Res.: Earth Surf.* **126**, e2021JF006172 (2021).
- [45] V. Bachelet, A. Mangeney, R. Toussaint, J. de Rosny, M. I. Arran, M. Farin, and C. Hibert, Acoustic emissions of nearly steady and uniform granular flows: A proxy for flow dynamics and velocity fluctuations, *J. Geophys. Res.: Earth Surf.* **128**, e2022JF006990 (2023).
- [46] P. Favreau, A. Mangeney, A. Lucas, G. Crosta, and F. Bouchut, Numerical modeling of landslides: Landslides and seismic waves, *Geophys. Res. Lett.* **37**, L15305 (2010).
- [47] L. Moretti, A. Mangeney, Y. Capdeville, E. Stutzmann, C. Huggel, D. Schneider, and F. Bouchut, Numerical modeling of the Mount Steller landslide flow history and of the generated long period seismic waves, *Geophys. Res. Lett.* **39**, L16402 (2012).
- [48] M. Yamada, A. Mangeney, Y. Matsushi, and L. Moretti, Estimation of dynamic friction of the akatani landslide from seismic waveform inversion and numerical simulation, *Geophys. J. Int.* **206**, 1479 (2016).
- [49] L. Moretti, A. Mangeney, F. Walter, Y. Capdeville, T. Bodin, E. Stutzmann, and A. Le Friant, Constraining landslide characteristics with Bayesian inversion of field and seismic data, *Geophys. J. Int.* **221**, 1341 (2020).
- [50] Y. Yan, Y. Cui, J. Guo, S. Hu, Z. Wang, and S. Yin, Landslide reconstruction using seismic signal characteristics and numerical simulations: Case study of the 2017 “6.24” Xinmo landslide, *Eng. Geol.* **270**, 105582 (2020).
- [51] H. An, C. Ouyang, and S. Zhou, Dynamic process analysis of the Baige landslide by the combination of DEM and long-period seismic waves, *Landslides* **18**, 1625 (2021).
- [52] H. A. Martin, A. Mangeney, A. Lefebvre-Lepot, B. Maury, and Y. Maday, An optimization-based discrete element model for dry granular flows: Application to granular collapse on erodible beds, <https://hal.archives-ouvertes.fr/hal-03790427> (2022).
- [53] S. Popinet, The basilisk code (2013).
- [54] F. Bouchut, A. Mangeney-Castelnaud, B. Perthame, and J.-P. Vilotte, A new model of Saint Venant and Savage–Hutter type for gravity driven shallow water flows, *C. R. Math.* **336**, 531 (2003).
- [55] F. Bouchut and M. Westdickenberg, Gravity driven shallow water models for arbitrary topography, *Commun. Math. Sci.* **2**, 359 (2004).
- [56] A. Mangeney-Castelnaud, F. Bouchut, J. Vilotte, E. Lajeunesse, A. Aubertin, and M. Pirulli, On the use of saint venant equations to simulate the spreading of a granular mass, *J. Geophys. Res.: Solid Earth* **110**, B09103 (2005).
- [57] M. Peruzzetto, A. Mangeney, F. Bouchut, G. Grandjean, C. Levy, Y. Thiery, and A. Lucas, Topography curvature effects in thin-layer models for gravity-driven flows without bed erosion, *J. Geophys. Res.: Earth Surf.* **126**, e2020JF005657 (2021).
- [58] J. J. Moreau, Unilateral contact and dry friction in finite freedom dynamics, in *Nonsmooth Mechanics and Applications*, International Centre for Mechanical Sciences, Vol. 302, edited by J. J. Moreau and P. D. Panagiotopoulos (Springer, Vienna, 1988), pp. 1–82.
- [59] M. Jean and J. J. Moreau, Unilaterality and dry friction in the dynamics of rigid body collections, in *Proceedings of the 1st Contact Mechanics International Symposium* (Presses Polytechniques et Universitaires Romandes, Lausanne, Switzerland, 1992).
- [60] J. J. Moreau, Numerical aspects of the sweeping process, *Comput. Methods Appl. Mech. Eng.* **177**, 329 (1999).
- [61] M. Jean, The non-smooth contact dynamics method, *Comput. Methods Appl. Mech. Eng.* **177**, 235 (1999).
- [62] J. J. Moreau, An introduction to unilateral dynamics, *Lecture Notes Appl. Comput. Mech.* **14**, 1 (2004).
- [63] L. Staron and E. J. Hinch, Study of the collapse of granular columns using two-dimensional discrete-grain simulation, *J. Fluid Mech.* **545**, 1 (2005).
- [64] M. Anitescu, Optimization-based simulation of nonsmooth rigid multibody dynamics, *Math. Program.* **105**, 113 (2006).
- [65] A. Tasora, D. Negrut, and M. Anitescu, Large-scale parallel multi-body dynamics with frictional contact on the graphical processing unit, *Proc. Inst. Mech. Eng., Part K: J. Multi-body Dyn.* **222**, 315 (2008).
- [66] F. Radjai and V. Richefeu, Contact dynamics as a non-smooth discrete element method, *Mech. Mater.* **41**, 715 (2009).
- [67] V. Acary, F. Cadoux, C. Lemaréchal, and J. Malick, A formulation of the linear discrete Coulomb friction problem via convex optimization, *Z. Angew. Math. Mech.* **91**, 155 (2011).
- [68] A. Seguin, A. Lefebvre-Lepot, S. Faure, and P. Gondret, Clustering and flow around a sphere moving into a grain cloud, *Eur. Phys. J. E* **39**, 63 (2016).
- [69] J. Léopoldès, X. Jia, A. Tourin, and A. Mangeney, Triggering granular avalanches with ultrasound, *Phys. Rev. E* **102**, 042901 (2020).
- [70] The Engineering Toolbox, [https://www.engineeringtoolbox.com/friction-coefficients-d\\_778.html](https://www.engineeringtoolbox.com/friction-coefficients-d_778.html) (2022), accessed Dec. 10, 2021.
- [71] H. Tang, R. Song, Y. Dong, and X. Song, Measurement of restitution and friction coefficients for granular particles and discrete element simulation for the tests of glass beads, *Materials* **12**, 3170 (2019).
- [72] A. Abramian, L. Staron, and P.-Y. Lagrée, The slumping of a cohesive granular column: Continuum and discrete modeling, *J. Rheol.* **64**, 1227 (2020).
- [73] GDR MiDi, On dense granular flows, *Eur. Phys. J. E* **14**, 341 (2004).
- [74] P. Jop, Y. Forterre, and O. Pouliquen, A constitutive law for dense granular flows, *Nature (London)* **441**, 727 (2006).
- [75] T. Barker, D. G. Schaeffer, P. Bohorquez, and J. M. N. T. Gray, Well-posed and ill-posed behaviour of the rheology for granular flow, *J. Fluid Mech.* **779**, 794 (2015).
- [76] E. D. Fernández-Nieto, J. Garres-Díaz, A. Mangeney, and G. Narbona-Reina, 2d granular flows with the  $\mu(I)$  rheology and side walls friction: A well-balanced multilayer discretization, *J. Comput. Phys.* **356**, 192 (2018).
- [77] M. Yamada, A. Mangeney, Y. Matsushi, and T. Matsuzawa, Estimation of dynamic friction and movement history of large landslides, *Landslides* **15**, 1963 (2018).
- [78] A. Guimpier, S. J. Conway, A. Mangeney, A. Lucas, N. Mangold, M. Peruzzetto, M. Pajola, A. Lucchetti, G. Munaretto, T. Sæmundsson, A. Johnsson, L. Le Deit, P. Grindrod, J. Davis, N. Thomas, and G. Cremonese, Dynamics of recent landslides (<20 My) on Mars: Insights from high-resolution topography on Earth and Mars and numerical modelling, *Planet. Space Sci.* **206**, 105303 (2021).



- [79] A. Mangeney, P. Heinrich, and R. Roche, Analytical solution for testing debris avalanche numerical models, *Pure Appl. Geophys.* **157**, 1081 (2000).
- [80] G. Faccanoni and A. Mangeney, Exact solution for granular flows, *Int. J. Numer. Anal. Meth. Geomech.* **37**, 1408 (2013).
- [81] A. Lucas, A. Mangeney, F. Bouchut, M.-O. Bristeau, and D. Mège, Benchmarking exercises for granular flows, in *The 2007 International Forum on Landslide Disaster Management* (Ho & Li, Hong Kong, 2007).
- [82] V. Gueugneau, K. Kelfoun, S. Charbonnier, A. Germa, and G. Carazzo, Dynamics and impacts of the May 8th, 1902 Pyroclastic current at Mount Pelée (Martinique): New insights from numerical modeling, *Front. Earth Sci.* **8**, 279 (2020).
- [83] J. L. Baker, T. Barker, and J. M. N. T. Gray, A two-dimensional depth-averaged  $\mu(I)$ -rheology for dense granular avalanches, *J. Fluid Mech.* **787**, 367 (2016).
- [84] J. M. N. T. Gray and A. N. Edwards, A depth-averaged  $(II)\mu(I)$ -rheology for shallow granular free-surface flows, *J. Fluid Mech.* **755**, 503 (2014).
- [85] C. Levy, A. Mangeney, F. Bonilla, C. Hibert, E. S. Calder, and P. J. Smith, Friction weakening in granular flows deduced from seismic records at the Soufrière Hills Volcano, Montserrat, *J. Geophys. Res.: Solid Earth* **120**, 7536 (2015).
- [86] J. Garres-Díaz, E. D. Fernández-Nieto, A. Mangeney, and T. M. de Luna, A weakly non-hydrostatic shallow model for dry granular flows, *J. Sci. Comput.* **86**, 1 (2021).
- [87] L. Vanel, D. Howell, D. Clark, R. P. Behringer, and E. Clément, Memories in sand: Experimental tests of construction history on stress distributions under sandpiles, *Phys. Rev. E* **60**, R5040(R) (1999).
- [88] M. Sperl, Experiments on corn pressure in silo cells—translation and comment of Janssen’s paper from 1895, *Granular Matter* **8**, 59 (2006).
- [89] B. P. Tighe and M. Sperl, Pressure and motion of dry sand: Translation of Hagen’s paper from 1852, *Granular Matter* **9**, 141 (2007).
- [90] T. Borykov, D. Mège, A. Mangeney, P. Richard, J. Gurgurewicz, and A. Lucas, Empirical investigation of friction weakening of terrestrial and Martian landslides using discrete element models, *Landslides* **16**, 1121 (2019).
- [91] L. Moretti, K. Allstadt, A. Mangeney, Y. Capdeville, E. Stutzmann, and F. Bouchut, Numerical modeling of the Mount Meager landslide constrained by its force history derived from seismic data, *J. Geophys. Res.: Solid Earth* **120**, 2579 (2015).
- [92] M. Peruzzetto, Numerical modeling of dry and water-laden gravitational flows for quantitative hazard assessment, Ph.D. thesis, Université de Paris, 2021.
- [93] S. Seabold and J. Perktold, Statsmodels: Econometric and statistical modeling with python, in *Proceedings of the 9th Python in Science Conference*, edited by S. van der Walt and J. Millman (2010).